Article

Hierarchical design of pseudosymmetric protein nanocages

https://doi.org/10.1038/s41586-024-08360-6

Received: 17 June 2023

Accepted: 6 November 2024

Published online: 18 December 2024

Open access

Check for updates

Quinton M. Dowling[1,2], Young-Jun Park[3], Chelsea N. Fries[2,3], Neil C. Gerstenmaier[2,3], Sebastian Ols[2,3], Erin C. Yang[2,3], Adam J. Wargacki[2,3], Annie Dosey[2,3], Yang Hsia[2,3], Rashmi Ravichandran[2,3], Carl D. Walkey[2,3], Anika L. Burrell[3], David Veesler[3,4], David Baker[2,3,4] & Neil P. King[2,3]✉

Discrete protein assemblies ranging from hundreds of kilodaltons to hundreds of megadaltons in size are a ubiquitous feature of biological systems and perform highly specialized functions[1,2]. Despite remarkable recent progress in accurately designing new self-assembling proteins, the size and complexity of these assemblies has been limited by a reliance on strict symmetry[3]. Here, inspired by the pseudosymmetry observed in bacterial microcompartments and viral capsids, we developed a hierarchical computational method for designing large pseudosymmetric self-assembling protein nanomaterials. We computationally designed pseudosymmetric heterooligomeric components and used them to create discrete, cage-like protein assemblies with icosahedral symmetry containing 240, 540 and 960 subunits. At 49, 71 and 96 nm diameter, these nanocages are the largest bounded computationally designed protein assemblies generated to date. More broadly, by moving beyond strict symmetry, our work substantially broadens the variety of self-assembling protein architectures that are accessible through design.

Self-assembling protein complexes are ubiquitous structures that are foundational to living systems. These structures vary in size from a few nanometres to micrometre-sized viral capsids and perform a wide variety of structural and biochemical functions[1,2]. The information that drives assembly of these complexes is encoded in their amino acid sequences and functionally takes the form of the structures of individual protein subunits and the interactions between them. The unique properties of self-assembling proteins have been exploited for applications in drug delivery, enzyme encapsulation and vaccines[4–7]. However, relying on naturally occurring assemblies constrains the engineer to existing sizes, shapes and levels of complexity. Methods for generating new self-assembling proteins render additional classes of structures and functions accessible, enabling these properties to be tailored to specific applications[8].

Advances in methods for controlling or designing the way protein subunits interact has led to an explosion of new designed assemblies in recent years, particularly those with finite, point-group symmetries[9] (that is, oligomers, nanocages and capsids). Engineered nanocages and capsids have been generated by computational protein design[10–14], rational design[15], genetic fusion and domain swapping[16–19], metal coordination[20–22] and laboratory evolution[23,24]. Each of these methods has a characteristic level of precision and predictive capacity. Computational docking and protein–protein interface design stands out for its ability to consistently create new protein complexes with atomic-level accuracy, although with a relatively modest success rate owing to the unique challenge posed by each interface design problem. Nevertheless, computationally designed protein nanocages have been engineered to encapsulate small molecules, nucleic acids and other polymers[25,26]; evolved for improved cargo packaging and extended in vivo half-life[25]; applied to enhance receptor-mediated signalling and virus neutralization[27,28]; and used as scaffolds for structure determination[29], multi-enzyme co-localization[30] and multivalent antigen presentation[31–34], including in multiple vaccines currently in clinical development[34,35] or licensed for use in humans[36,37]. Further development of computational methods will give rise to designed protein nanomaterials of continually increasing sophistication, leading to improved performance in these applications and making additional applications possible.

Design methods reported to date have relied on the use of strict symmetry and pre-existing oligomeric building blocks to reduce the number of new interfaces that must be designed[3,38]. Although this approach yields access to a handful of finite (that is, bounded) symmetric architectures that require only a single designed interface[39], it nevertheless places a severe constraint on the architectures that are accessible to design and their size and complexity. The largest and most complex structures designed using this approach comprise 120 subunits and have strict icosahedral symmetry, featuring a single copy of each of two subunits in the icosahedral asymmetric unit[11,32]. Developing methods for breaking the symmetry of computationally designed protein assemblies is a key next step in developing more sophisticated self-assembling proteins.

Four routes to larger and more sophisticated protein assemblies exist, each of which is observed in naturally occurring self-assembling proteins. First, larger protein subunits could be used as building blocks, with titin providing an extreme example[40]. However, this approach is untenable as a general solution, as limits in protein

[1]Department of Bioengineering, University of Washington, Seattle, WA, USA. [2]Institute for Protein Design, University of Washington, Seattle, WA, USA. [3]Department of Biochemistry, University of Washington, Seattle, WA, USA. [4]Howard Hughes Medical Institute, Seattle, WA, USA. ✉e-mail: neilking@uw.edu

translation, folding, stability and flexibility are quickly encountered[2]. Second, the number of different kinds of subunits in the assembly (or its asymmetric unit (asu)) could be increased by designing new asymmetric interactions between them, as observed in multi-subunit molecular machines such as RNA polymerases[41]. Although ultimately we expect this approach to become possible, it is currently impractical, as it would compound the low success rates of existing interface design methods. Third, principles of quasi-equivalence could be used to design large assemblies from protein subunits that adopt subtly different conformations depending on their local symmetry environment, a phenomenon commonly found in icosahedral virus capsids[23,42,43]. However, current computational protein design methods lack the precision required to reliably encode in a single amino acid sequence the multiple subtly different backbone conformations required to implement this approach. Finally, pseudosymmetry could be used to enable asymmetric functionalization of oligomeric building blocks, opening up new routes to the design of larger assemblies. Pseudosymmetry is also frequently observed in icosahedral virus capsids, where genetically distinct subunits or domains adopt roughly symmetric orientations within oligomeric capsomers[44]. For example, pseudosymmetric trimers in virus capsids may comprise three subunits, each containing two related but slightly distinct domains that result in an (A–B)–(A–B)–(A–B) arrangement with roughly sixfold symmetry at the backbone level[45,46]. Such trimers can be arranged in hexagonal lattices that form the facets of very large icosahedral assemblies; the A and B domains form the distinct sets of contacts that are necessary to form non-porous lattices. Although designing pseudosymmetric assemblies requires the creation of multiple new protein–protein interfaces, a hierarchical approach in which pseudosymmetric oligomers are designed first and subsequently used as the building blocks of larger pseudosymmetric assemblies would enable the distinct interfaces to be designed and validated individually. This approach avoids compounding the relatively high failure rate of interface design and, as we show, permits the design of novel cage-like protein nanomaterials that far exceed the size and complexity of previously designed assemblies.

Pseudosymmetric heterotrimer design

We started our pseudosymmetric design with a homotrimeric aldolase from the hyperthermophilic bacterium *Thermotoga maritima* that is remarkably stable and tolerant of modification (Protein Data Bank (PDB) ID 1WA3; ref. 47). This trimer has previously been used to design multiple one- and two-component protein assemblies[11,14], which as we show below, makes possible the re-use of these previously designed interfaces in the creation of large pseudosymmetric assemblies. We set out to identify the minimum set of mutations necessary to drive formation of a pseudosymmetric heterotrimer. We used two methods to identify individual mutations predicted to disrupt—as well as compensatory mutations predicted to restore—homotrimer stability, reasoning that combining sets of such mutations across three variants of the trimer subunit could yield pseudosymmetric heterooligomers (Fig. 1a). First, the energetic effects of all possible single and pairwise mutations in 98 contacting residue pairs over 36 positions in the 1WA3 homotrimer interface were evaluated using Rosetta. Ninety-six unique individual mutations increased the predicted homotrimerization energy (ddG) or Rosetta score by more than 100 Rosetta energy units, suggesting that they may disrupt the wild-type homotrimeric interface (Extended Data Fig. 1a,b). Only a subset of these had compensatory mutations that brought the normalized total score or normalized ddG close to zero; these were considered further (Fig. 1b,c, red boxes). Second, because 1WA3 is a naturally occurring protein, we also used bioinformatics to guide our mutant and double-mutant selection. Using GREMLIN[48,49], we inspected the coupling matrices of highly co-evolving residues at the trimer interface to identify low-frequency single mutations (for example, H91I; PDB ID 1WA3 numbering) with high-frequency compensatory mutations (for example, V118Y) (Fig. 1d). As expected, many of the predicted disrupting mutations identified by both methods were mutations to bulky hydrophobic residues (Fig. 1e). Models of those single mutants were visually inspected and then paired with the best-scoring double mutant. In total, mutations from 76 mutant pairs were selected for experimental screening (Extended Data Table 1).

First, the ability of each single mutation to disrupt trimer formation was screened in a lysate-based assay by evaluating its effect on the assembly of I53-50, a previously reported two-component nanocage[11] comprising a trimeric component (I53-50A) derived from 1WA3 and a pentameric component (I53-50B) derived from a bacterial lumazine synthase[50] (PDB ID 2OBX). When I53-50A and I53-50B are mixed, the two components spontaneously self-assemble to form a 120-subunit complex. Clarified lysates from *Escherichia coli* that express the I53-50A mutants were mixed with purified I53-50B pentamer at three different pentamer concentrations and analysed by native (non-denaturing) PAGE (Fig. 1f). The 1WA3 trimer proved remarkably plastic: only 3 out of the 82 single mutants tested did not yield a band corresponding to the assembled I53-50 nanocage, indicating that these either prevented soluble expression of the trimer variant or altered its geometry so that it was no longer assembly-competent. Mutations that prevented nanocage formation were then combined with their compensatory mutation to determine whether the combination restored the ability to form I53-50 nanocages (Extended Data Fig. 1c). Through these analyses, three pairs of functional disrupting and compensatory mutations were identified: H91I/V118Y, P90F/P147A and P114F/F131V.

We initially set out to generate an 'ABC' heterotrimer, in which each subunit has a different amino acid sequence, by combining the three mutant pairs in a tricistronic expression construct (all novel amino acid sequences provided in Supplementary Table 1). We introduced one of the homotrimer-disrupting mutations into each subunit: V118Y into A, P90F into B and P114F into C (Fig. 1g). The disrupting mutations in the A and C chains clashed with the neighbouring subunit in a 'clockwise' direction, whereas P90F in the B chain clashed with its 'anticlockwise' neighbour. As a result, the three compensatory mutations were added to the B (F131V) and C (H91I and P147A) chains. This generated two new interfaces predicted to be orthogonal to the wild-type interface, in principle providing the three interfaces required to form a heterotrimer. However, when we co-expressed the three proteins and purified them by immobilized metal affinity chromatography (IMAC) and StrepTrap chromatography, SDS–PAGE analysis suggested the presence of trimers comprising predominantly a mixture of the A and B subunits, with little of the C subunit (Extended Data Fig. 1d–f). To better understand this off-target species, we expressed a bicistronic gene containing only the A and B subunits. We purified the resulting protein and identified two distinct trimeric assemblies by native mass spectrometry: a trimer comprising one copy of the A chain and two copies of the B chain ('ABB'), as well as a trimer comprising two copies of the A chain and one copy of the B chain ('AAB') (Fig. 1h and Extended Data Fig. 1g,h). Although initially unexpected, we suspected that the remarkable plasticity of the 1WA3 trimer allowed it to tolerate the disrupting mutations in the A and B chains when these were combined with the compensatory mutation F131V, a suspicion that was borne out in later structural studies. Although not the intended ABC heterotrimer, we realized that these heterotrimers were probably pseudosymmetric and, as we describe below, could provide a simple route to designing large pseudosymmetric materials. To confirm that symmetry was preserved at the backbone level—a prerequisite for our hierarchical design approach—we determined whether the heterotrimer mixture was assembly-competent by purifying and incubating it in a 1:1 molar ratio with I53-50B pentamer. Assemblies were purified by size-exclusion chromatography (SEC) and nanocages with the known I53-50 morphology[11] were observed by negative-stain electron microscopy (Fig. 1i).

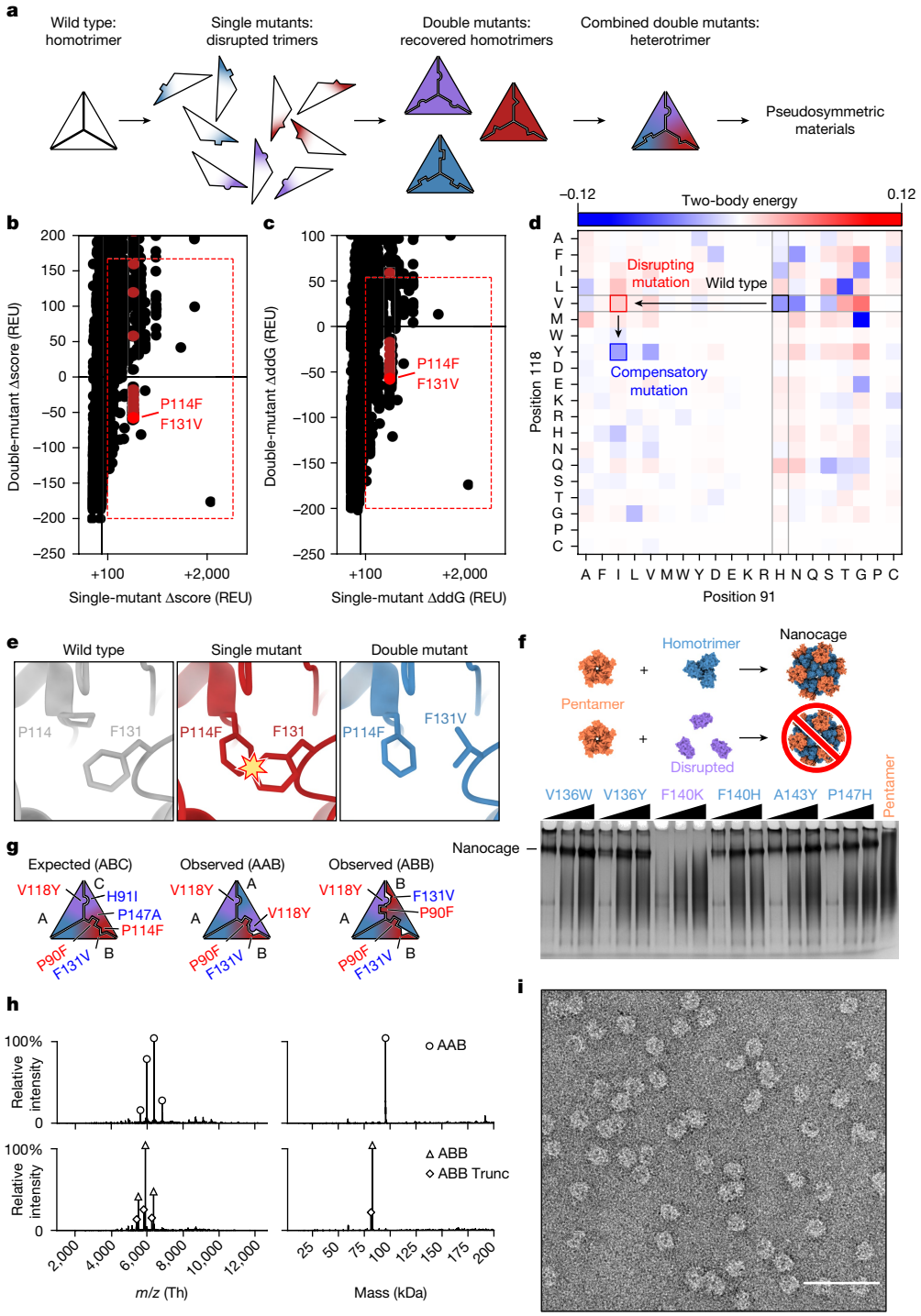

Fig. 1 | Design and characterization of a pseudosymmetric heterotrimer. **a**, The design protocol starts with a homotrimer to which single trimer-disrupting mutations are introduced, followed by compensatory mutations that rescue trimer assembly. Sets of orthogonal mutations (depicted as red, purple and blue) are combined to generate a heterotrimer that can then be used as a component in pseudosymmetric materials. **b**,**c**, Calculated changes in Rosetta score (Δscore) (**b**) and predicted trimerization energy (ΔddG) (**c**) upon mutation were used to evaluate single mutants (horizontal axis) and double mutants (vertical axis). The red boxes enclose mutants that met selection criteria for further evaluation, and mutant pairs containing P114F, shown in **e**, are highlighted in red. REU, Rosetta energy units. **d**, Possible mutations were also evaluated by their co-evolution coupling matrix. Desirable mutations are those for which the single-mutant–wild-type pair is observed less frequently than expected (red; H91I/V118) and the double-mutant pair is observed more frequently than expected (blue; H91I/V118Y). **e**, An example of a productive mutant pair in which the wild-type residue F131 clashes with the mutant residue P114F and the second mutation F131V resolves the clash. **f**, Disruption of trimer geometry was assayed by assembling mutant I53-50A trimers in clarified *E. coli* lysates with purified I53-50B pentamer and evaluating the presence or absence of I53-50 nanocages by native PAGE. Here, F140K was identified as a disrupting single mutation. Black wedges indicate increasing pentamer concentration in the assembly reaction. Data are representative of three independent experiments. For gel source data, see Supplementary Fig. 1. **g**, Diagram of the expected ABC heterotrimer and the observed AAB and ABB heterotrimers. Disrupting mutations are labelled in red and compensatory mutations are in blue. **h**, Native mass spectrometry of AAB-enriched (top) and ABB-enriched (bottom) heterotrimer fractions purified by IMAC and SEC. ABB Trunc refers to a truncation product of the A chain in which the N-terminal ten residues of the protein were missing. **i**, Assembly of I53-50-like nanocages using an AAB/ABB mixture of I53-50A heterotrimer was verified by negative-stain electron microscopy. Scale bar, 100 nm.

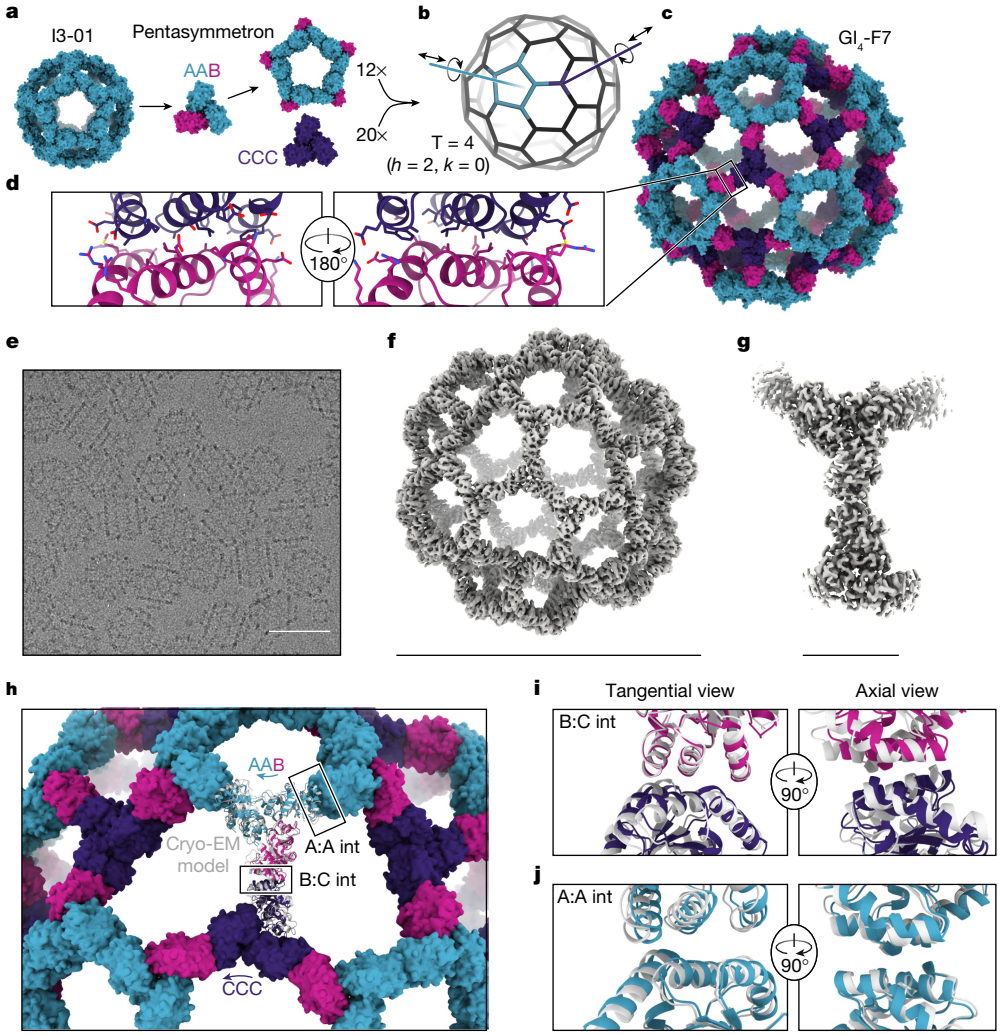

Fig. 2 | Design and characterization of the 240-subunit GI_4-F7 nanocage. **a**, Schematic of pentasymmetron generation from I3-01 and the AAB heterotrimer. The A (cyan) subunits in the pentasymmetron retain the two-fold symmetric I3-01 nanocage interface, whereas the B (magenta) subunits are available for docking. **b**, Docking the pentasymmetron as a rigid body against CCC homotrimers (purple) yields 240-subunit, T = 4 assemblies. Translational and rotational degrees of freedom for the pentasymmetron and homotrimer components are indicated. **c**, A design model of GI_4-F7. **d**, Detail of the computationally designed interface between the B and C subunits of GI_4-F7 design model. **e**, Cryo-EM micrograph of assembled GI_4-F7 nanocages embedded in vitreous ice. Scale bar, 50 nm **f**, The 4.4 Å resolution density map of the entire GI_4-F7 nanocage. Scale bar, 49 nm. **g**, The 3.1 Å resolution density map from an asu obtained via symmetry-expansion and local refinement. Scale bar, 7.4 nm. **h**, Comparison of the cryo-EM structure derived from local refinement (grey ribbon) with the computational design model (coloured ribbons), aligned using a single copy of the asu. Arrows indicate rigid-body deviations of the pentasymmetron (cyan) and CCC homotrimer (purple). Int, interface. **i**,**j**, Detail of the rigid-body deviations from the design model at the B–C interface (**i**) and the A–A (I3-01) interface (**j**). In **j**, two neighbouring copies of the AAB heterotrimer from the full nanocage reconstruction and the design model were aligned.

Design of a 240-subunit nanocage

We then used the pseudosymmetric heterotrimers to design large, pseudosymmetric assemblies with icosahedral symmetry. We had previously used the 1WA3 homotrimer to generate a single-component nanocage with icosahedral symmetry, I3-01, by designing a novel protein–protein interface with two-fold symmetry between the subunits of adjacent trimers[14]. The existence of this interface enabled us to generate a 15-subunit 'pentasymmetron' comprising 5 trimers by simply including the I3-01 mutations on the A chains of the AAB heterotrimer (Fig. 2a). Docking this pentasymmetron against C3-symmetric homotrimers ('CCC') and designing novel sequences that create favourable interfaces between the B and C chains yielded models of 240-subunit nanocages with icosahedral symmetry (Fig. 2b–d). The Caspar–Klug triangulation (T) number notation[42] is useful for describing these pseudosymmetric nanocages, although the assignment of subunits to geometric elements is different than in traditional use of the T number in structural virology. In our pseudosymmetric nanocages, trimeric building blocks form wireframe-like structures surrounding roughly pentagonal and hexagonal pores, with each subunit interacting with exactly one other subunit from a different trimer. The original I3-01 nanocage can be thought of as T = 1, with one (A) subunit in the asu, while the pentasymmetron-containing 240-subunit nanocages are T = 4, with four (2×A, 1×B, 1×C) subunits in the asu. In these assemblies $k = 0$, so the T number is equal to h^2, where h is a positive integer that represents the number of steps required to traverse from one pentasymmetron to another, each step moving to the next pentagonal or hexagonal pore. Because this is one of the set of equations used to define class I Goldberg polyhedra[51], we refer to these nanocages using the naming convention GI_T-X, where G stands for Goldberg, I for icosahedral symmetry, T is used to denote the triangulation number of a particular architecture, and X is a unique identifier for each design. We expressed three initial designs

in *E. coli* as tricistronic genes with a 6×His tag on only the C chain, and found that Ni^{2+} beads co-precipitated all three subunits of two of the designs, suggesting assembly (Extended Data Fig. 2a–c). We proceeded with the better expressing and more soluble of the two, GI_4-F7. To scale up expression of the AAB heterotrimer so that we could explore assembly of GI_4-F7 in vitro from purified components, we re-cloned it as a bicistronic AB construct with a 6×His tag on the A chain. Upon gradient elution during IMAC, we observed three peaks corresponding to an ABB-rich fraction, an AAB-rich fraction and off-target AAA homotrimers that assembled to an I3-01-like nanocage (Extended Data Fig. 2d). We polished the AAB and ABB fractions by SEC, discarding the I3-01-like nanocage fraction (Extended Data Fig. 2e–g). This step removed the I3-01-like assemblies but did not resolve the ABB and AAB trimers. We therefore expected some cross-contamination between those trimer species, as observed in the native mass spectrometry data (Fig. 1h). In parallel, we purified 6×His-tagged CCC homotrimer—which was also derived from the 1WA3 trimer—by IMAC and SEC.

We mixed the AAB heterotrimer with an excess of the CCC homotrimer in the presence of detergent and initiated assembly by dialysing overnight into Tris-buffered saline (Methods). The major assembly product was purified by SEC (Extended Data Fig. 2h), and images obtained by cryo-electron microscopy (cryo-EM) of vitrified specimens revealed wireframe structures with large hexagonal pores that closely resembled the design model (Fig. 2e). We determined a single-particle reconstruction of GI_4-F7 at 4.4 Å resolution applying icosahedral symmetry and a 3.1 Å resolution structure of the 4 chains of the asu (cryo-EM processing details in Extended Data Fig. 3 and Extended Data Table 2). The cryo-EM structure agrees well with the design model, with a Cα root mean-squared deviation (r.m.s.d.) of 9.3 Å across all 240 subunits and 3.0 Å within the asu (Fig. 2f,g and Extended Data Fig. 4). The differences between the cryo-EM structure and design model are mostly accounted for by slight rigid-body deviations allowed by the limited degrees of freedom of the oligomeric building blocks in this symmetric architecture (Extended Data Fig. 4a). The main rigid-body deviation is a 5.9° clockwise rotation of the pentasymmetron, accompanied by a 5.8 Å translation away from the origin (Fig. 2h). The CCC homotrimer compensates by rotating 12.4° and translating 4.0 Å, resulting in only slight local shifts relative to the design model (2.1 Å across the B:C subunits; Fig. 2i). Within the pentasymmetron, the degrees of freedom of the AAB heterotrimer are no longer restricted by the strict icosahedral symmetry of I3-01, resulting in a slight deviation from perfect two-fold symmetry between neighbouring A chains (1.4 Å Cα r.m.s.d.; Fig. 2j and Extended Data Fig. 4d). In addition to these slight rigid-body deviations, the 3.1 Å resolution structure of the asu enabled us to visualize the pseudosymmetry-generating mutations in the A and B subunits. As suspected, we observed backbone and sidechain rearrangements within each protomer that explained how the V118Y and P90F disrupting mutations were tolerated in the AAB heterotrimer. Specifically, we saw that the loop containing H91 and the entire preceding helix shifted relative to the design model in all three subunits. This created enough space to accommodate the P90F mutation in chain B and for V118Y in the A subunits to pack against H91 (Extended Data Fig. 4e,f). Additional minor structural deviations were observed within each subunit, primarily in the B:C interface (Extended Data Fig. 4g–j). Overall, the diameter of GI_4-F7 observed by cryo-EM is within 2% of the design model, establishing that our method is capable of accurately designing pseudosymmetric protein nanomaterials comprising hundreds of subunits.

Observation of a 540-subunit nanocage

Unexpectedly, in a number of the GI_4-F7 micrographs we also observed a 71-nm nanocage with a similar wireframe morphology and hexagonal pores (Fig. 3a). By counting the hexagonal pores we found that $h = 3$; thus the nanocage is T = 9 and we refer to it as GI_9-F7. GI_9-F7 can be explained by the presence of small amounts of ABB heterotrimer in AAB heterotrimer preparations. Analogous to the AAB heterotrimer, which forms a pentasymmetron through five roughly two-fold-symmetric A:A interfaces inherited from I3-01, the ABB heterotrimer forms a two-trimer 'disymmetron' structure held together by the same A:A interaction (Fig. 3b). In GI_9-F7 this disymmetron occupies the icosahedral two-fold symmetry axes, providing the edges that connect three-fold-symmetric facets containing three ABB heterotrimers and three CCC homotrimers. As a result, GI_9-F7 is quasisymmetric in addition to being pseudosymmetric: the A, B and C subunits each occupy multiple, distinct environments in the assembly. We expanded GI_4-F7 to generate a design model for GI_9-F7 containing 12 pentasymmetrons constructed from AAB heterotrimers, 30 disymmetrons comprising ABB heterotrimers, and 60 CCC homotrimers (Fig. 3b). The asu of GI_9-F7 therefore comprises one AAB trimer, one ABB trimer and one CCC trimer. To generate more homogenous preparations of GI_9-F7, we separately polished the AAB and ABB heterotrimer fractions from IMAC (Methods) and assembled them with CCC homotrimer at a 1:1:1 ratio. Micrographs of SEC-purified GI_9-F7 assemblies revealed enrichment of the target assembly (Extended Data Fig. 5a), and we determined a cryo-EM structure of the nanocage to 6.7 Å resolution applying icosahedral symmetry, as well as a 4.0 Å resolution structure of the asu (Fig. 3c, Extended Data Fig. 3 and Extended Data Table 2). Consistent with the accuracy with which we designed GI_4-F7, the GI_9-F7 cryo-EM structure deviates from the design model by only 11.5 Å Cα r.m.s.d. across all 540 subunits, 1.6% of the nanocage diameter, and superimposition of the designed asu with the structure yields a Cα r.m.s.d. of 4.6 Å across all 9 chains.

Although the pentasymmetron, disymmetron and three homotrimers in GI_9-F7 are constrained by the five-fold, two-fold and three-fold icosahedral symmetry axes, respectively, no single trimer occupies a position constrained by icosahedral symmetry—the icosahedral three-fold instead passes through a large pore. Each trimer can therefore deviate from the design model along all six rigid-body degrees of freedom. As a result, the two designed nanocage interfaces (B:C and A:A) occupy five quasi-equivalent positions in GI_9-F7. Two of the B:C interfaces are located within the icosahedral asu, between the CCC homotrimer and the B chain of a neighbouring pentasymmetron (interface 1) or disymmetron (interface 2) (Fig. 3d). The third B:C interface is between the CCC homotrimer and the B chain of a disymmetron in a neighbouring asu (interface 3). Despite being unconstrained by symmetry, interfaces 1 to 3 fit well to the density, with a very small deviation from the design model comprising only a small rotation with very little radial translation (Fig. 3e and Extended Data Fig. 5b–f). Interfaces 4 and 5 are the A:A (that is, I3-01) interfaces in the pentasymmetron and disymmetron, respectively (Fig. 3f). Unlike interfaces 1 to 3, interfaces 4 and 5 appear to differ, with a Cα r.m.s.d. of 1.3 Å to each other and Cα r.m.s.d. values of 2.0 and 2.4 Å to the GI_9-F7 design model, respectively (Fig. 3g and Extended Data Fig. 5g–i). This difference arises because the pentasymmetron interface (interface 4) is not symmetrically constrained, while the disymmetron interface (interface 5) is constrained by the icosahedral two-fold symmetry axis. We propose that the lowest-energy state of the A:A interface is not perfectly symmetric, but that the symmetry requirements for nanocage assembly force it to adopt a higher-energy, two-fold-symmetric configuration where appropriate.

To gauge the potential utility of GI_4- and GI_9-F7 as scaffolds for nanoparticle vaccines, we multivalently displayed the receptor-binding domain (RBD) of the SARS-CoV-2 spike protein on them and measured their ability to activate RBD-specific B cells. We conjugated SpyTagged RBD to GI_4-F7 and GI_9-F7 nanocages bearing SpyCatcher[52] as a genetic fusion on the CCC subunit, yielding a theoretical maximum of 60 and 180 RBDs per nanocage, respectively. Efficient covalent linkage was verified by SDS–PAGE, with excess RBD–SpyTag but no residual CCC–SpyCatcher visible (Fig. 3h). Intact nanocages of the expected size and

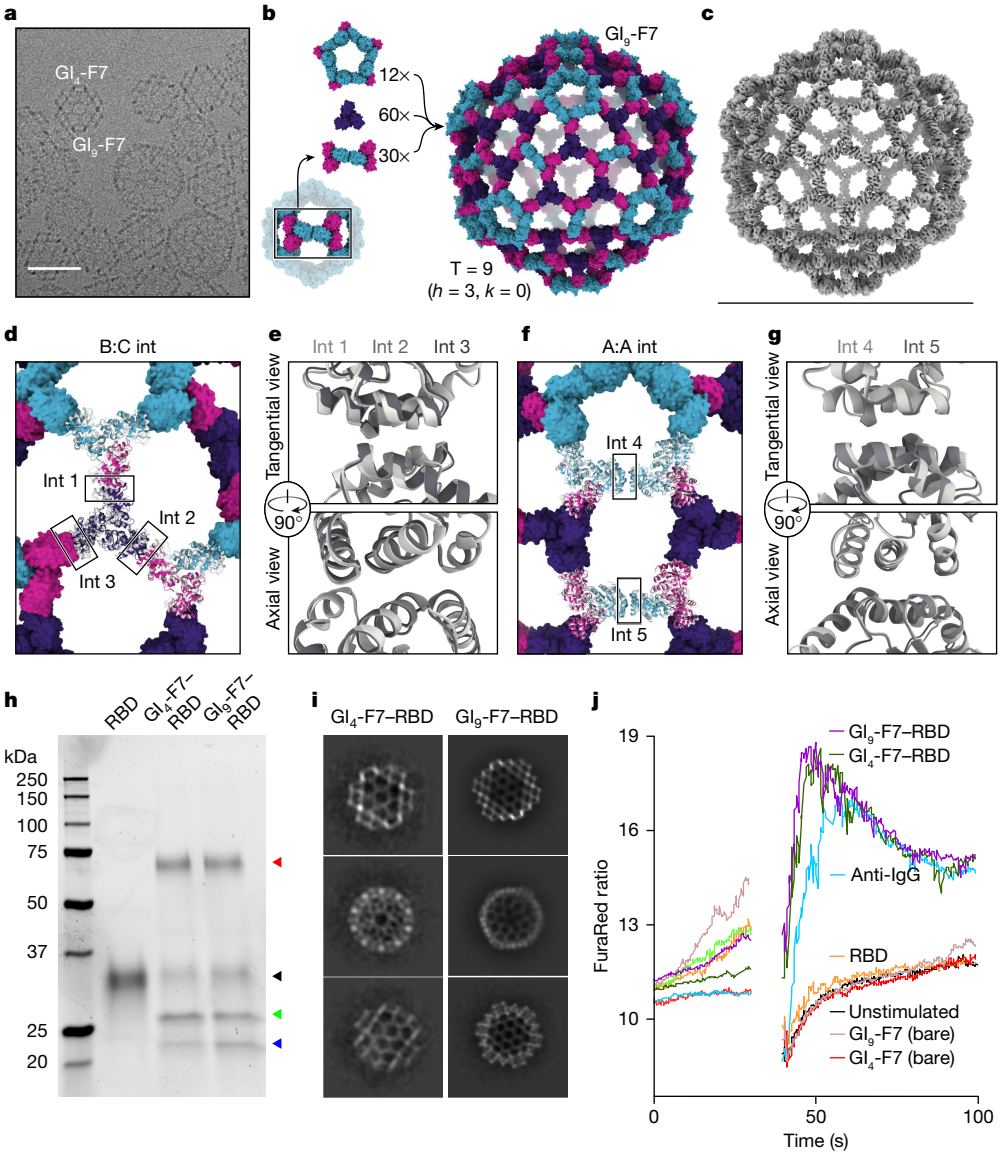

Fig. 3 | Discovery and characterization of the 540-subunit GI_9-F7 nanocage. **a**, A cryo-electron micrograph showing GI_4-F7 and GI_9-F7 nanocages in the same preparation. Scale bar, 50 nm. **b**, Design model of GI_9-F7, constructed from 12 pentasymmetrons, 60 CCC homotrimers and 30 disymmetrons. A subunits, cyan; B subunits, magenta; C subunits, purple. **c**, Cryo-EM map of GI_9-F7 at 6.7 Å resolution. Scale bar, 71 nm. **d**, Comparison of a model derived from the cryo-EM map (grey) with the computational design model (other colours), aligned using a single asu (shown in cartoon). The three independent copies of the B:C interface in the asu are indicated. **e**, Alignment of int 1 (light grey), int 2 (medium grey) and int 3 (dark grey) from the cryo-EM model. **f**, Alignment of two neighbouring copies of AAB heterotrimers from the cryo-EM model to the design model. The two independent copies of the A:A (I3-01) interface, located in the pentasymmetron (int 4) and the disymmetron (int 5), are indicated. **g**, Alignment of the two A:A (I3-01) interfaces from the cryo-EM model, int 4 (light grey) and int 5 (medium grey). **h**, SDS–PAGE of antigen-bearing GI_4-F7 and GI_9-F7 nanocages. RBD–SpyTag (left lane) was conjugated to CCC–SpyCatcher in either GI_4-F7 or GI_9-F7 nanocages. Red arrowhead, conjugated CCC–RBD; black arrowhead, residual RBD–SpyTag; green arrowhead, A subunit from AAB and ABB and B subunit from BBB; blue arrowhead, B subunit from AAB and ABB. For gel source data, see Supplementary Fig. 5. **i**, Representative 2D class averages from negative-stain electron microscopy of RBD-conjugated GI_4-F7 or GI_9-F7 nanocages. **j**, Representative plot of Ca^{2+} flux induced by BCR signalling in RAMOS cells that stably express the SARS-CoV-2 spike-specific antibody COVA2-15 as an IgG BCR[60]. Cell lines were stimulated with various antigens with 4 μg ml^{-1} RBD after reading a 30 s baseline. Data are representative of two independent experiments.

morphology were observed by negative-stain electron microscopy, although the displayed antigen could not be seen owing to its small size and flexible linkage to each nanocage (Fig. 3i). We then measured Ca^{2+} flux in B cells bearing an RBD-specific B cell receptor (BCR) after treatment with the RBD nanocages, comparing this against monomeric RBD–SpyTag, 'bare' nanocages lacking displayed RBD and an anti-IgG positive control that specifically cross-links the transgenic BCRs and provides an estimate of maximal BCR signalling in the assay (Supplementary Fig. 6). The monomeric SpyTag and bare nanocages did not induce BCR signalling above background, whereas the anti-IgG efficiently induced signalling as expected (Fig. 3j). Activation by both RBD-bearing nanocages was more robust than by the anti-IgG control, peaking both faster and higher. These data show that antigen-bearing pseudosymmetric nanocages efficiently activate B cells, suggesting their potential utility as vaccine scaffolds.

Generation of extensible nanocages

The geometries of I3-01 GI_4-F7, and GI_9-F7 are analogous to the first three instances in the infinite series of class I Goldberg polyhedra[42,51].

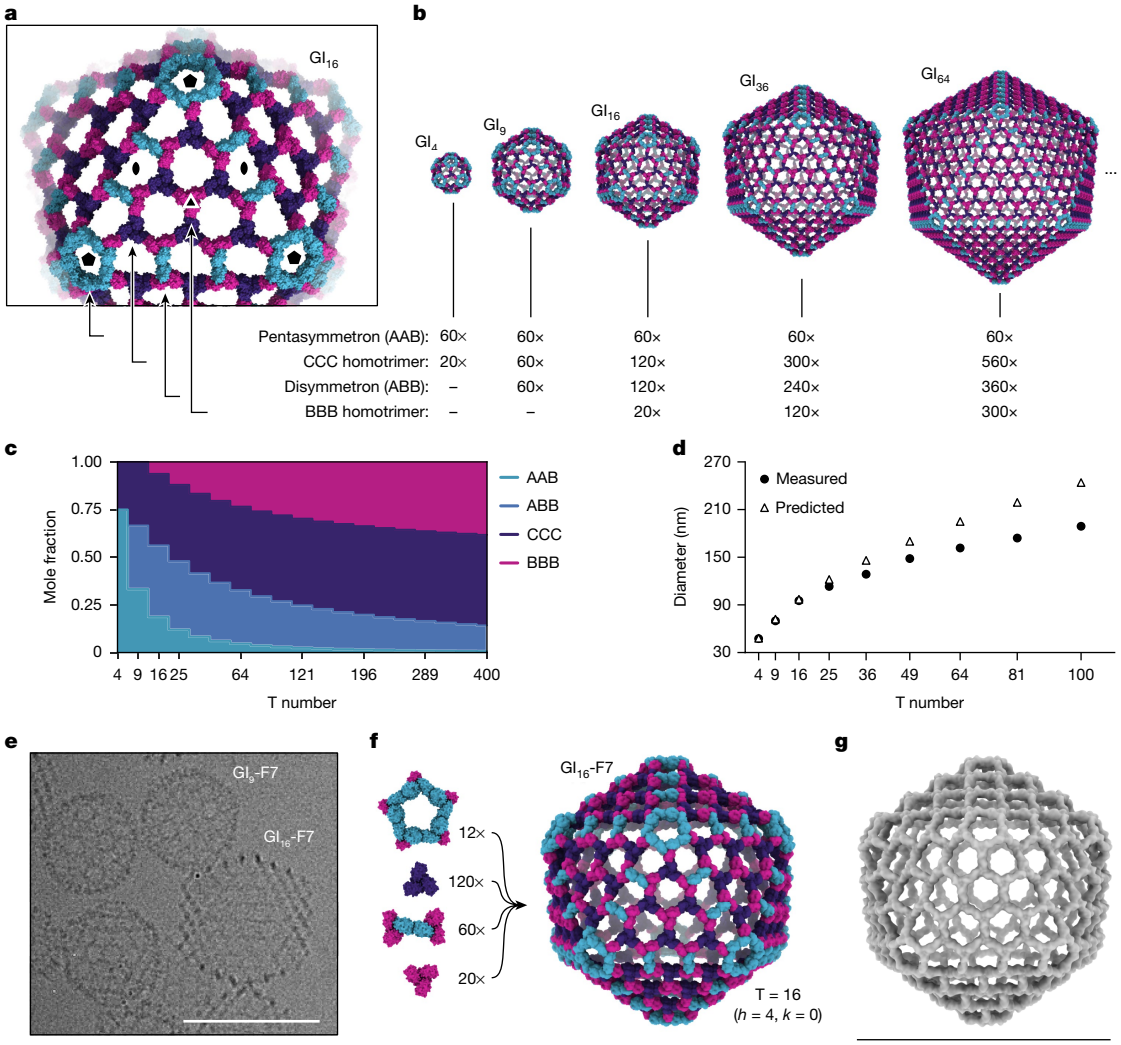

Fig. 4 | Generation of pseudosymmetric nanocages with extensible hexagonal lattice facets. a, The four types of trimers required to generate pseudosymmetric nanocages with T numbers ≥16, viewed in the context of the GI_{16}-F7 design model. Icosahedral five-fold, two-fold and three-fold symmetry axes are indicated. **b**, Design models and corresponding building block stoichiometries of GI_4-F7, GI_9-F7, GI_{16}-F7, GI_{36}-F7 and GI_{64}-F7 nanocages. The stoichiometries listed indicate the number of each kind of trimeric component. **c**, Graphical depiction of trimer stoichiometry as a function of T number. **d**, Theoretical nanocage diameters and *Z*-average hydrodynamic diameters measured by DLS as a function of trimer stoichiometry used during in vitro assembly (indicated by T number). Data are representative of two independent experiments. **e**, Cryo-electron micrograph of a sample containing GI_9-F7 and GI_{16}-F7 nanocages. Scale bar, 100 nm. **f**, Composition and design model of the GI_{16}-F7 nanocage. **g**, The 14.9 Å resolution cryo-EM map of GI_{16}-F7. Scale bar, 96 nm.

The larger instances in this series are effectively constructed by folding 20 roughly triangular 2D hexagonal lattices into icosahedron-like shapes through the introduction of curvature at their edges and vertices. Theoretically, the next nanocage in the series would be GI_{16}-F7. As in GI_4-F7 and GI_9-F7, curvature in this structure would be provided by disymmetrons and pentasymmetrons. However, GI_{16}-F7 would have a C3-symmetric component centred on the icosahedral three-fold symmetry axis, as opposed to the pore-centred three-fold of GI_9-F7. Extrapolating from GI_4-F7 and GI_9-F7, this component must be a homotrimer of the B chain ('BBB'), and it must be coplanar with the six surrounding CCC homotrimers (that is, their three-fold axes must be parallel; Fig. 4a). Nanocages beyond GI_{16}-F7 simply add more copies of the BBB and CCC homotrimers (and ABB disymmetrons) to form larger two-dimensional hexagonal arrays (Fig. 4b). Thus, obtaining GI_{16}-F7 and the larger nanocages in the series does not require new interface design, only production of BBB homotrimer. Indeed, analysing an equimolar mixture of purified BBB and CCC homotrimers by negative-stain electron microscopy yielded a 2D array with a characteristic hexagonal lattice diffraction pattern (Extended Data Fig. 6a–c). The dimensions of the array agree well with a design model derived from the GI_9-F7 nanocage (Extended Data Fig. 6d,e).

In the absence of other control mechanisms, the inclusion of BBB homotrimer in assembly reactions should yield distributions of large T number assemblies rather than monodisperse preparations of a single species. However, the relative stoichiometries of the components in each assembly vary as a function of T number (Fig. 4b,c), providing a potential mechanism for modulating assembly size. We prepared assembly reactions containing the 4 components at the stoichiometries corresponding to T = 4, 9, 16, 25, 36, 49, 64, 81 and 100 nanocages. Consistent with our predictions, the *Z*-average hydrodynamic diameter measured by dynamic light scattering (DLS) increased with increasing target T number (from 47.5 ± 0.4 nm to 188 ± 1.1 nm), though the observed hydrodynamic diameter deviated from the predicted diameter at higher T numbers (Fig. 4d and Extended Data Table 3). This deviation could be due to contaminating AAB trimer in the ABB fraction (Extended Data Fig. 2d), which would be expected to favour

the lower T number assemblies in which AAB is more prevalent. Furthermore, smaller assemblies will be kinetically favoured over larger assemblies, which could bias the resulting particle distribution. GI_{16}-F7 was readily observed by cryo-EM in assembly reactions prepared at the T = 16 stoichiometry (Fig. 4e). GI_{16}-F7 is predicted to have a diameter of 96 nm and contains 12 pentasymmetrons, 120 CCC homotrimers, 60 disymmetrons and 20 BBB homotrimers for a total of 960 subunits (Fig. 4f). We determined a 14.9 Å resolution cryo-EM map of GI_{16}-F7 and found that it closely matches the expected geometry of the design (Fig. 4g). This assembly has an internal volume that is roughly 90-fold larger than our previously designed nanocages with strict icosahedral symmetry[11,14] and adeno-associated viruses, commonly used vectors for gene therapy[53].

Conclusions

Here we show that designing pseudosymmetric protein building blocks, in which symmetry is broken at the sequence level while backbone symmetry is maintained, enables the construction of very large pseudosymmetric protein nanocages. This work moves beyond established methods for accurately designing novel self-assembling proteins[10,11,14,54], as it breaks their reliance on strict symmetry and provides a route to a large set of architectures that were previously inaccessible to design. Although both the previous and current methods are general with respect to the choice of building block and can therefore give rise to rich varieties of potential assemblies, the space of asymmetric architectures is vastly larger than that of strictly symmetric structures.

For this work, we used a hyperstable protein from a thermophilic organism as a building block, as many studies have shown that stable proteins are more tolerant of modification[55]. Although this choice contributed to the successful expression of a large number of mutants, it also led to the low success rate of symmetry-breaking mutations: 1WA3 proved remarkably resilient to mutations intended to disrupt the homotrimer. Key to our success was having an efficient screen for connecting genotype to phenotype (in this case, maintenance of backbone symmetry), which we achieved by selecting a building block that had already been used as a component in a larger symmetric assembly. Although at present this approach may limit the use of our experimental screen to a subset of known protein oligomers, our overall design strategy in theory generalizes to any oligomeric protein. We expect this limitation to further diminish as methods for protein structure prediction and design continue to yield improved success rates, which will enable the generation of increasingly asymmetric protein nanomaterials (see the accompanying Article[56]).

Although some small viruses make purely pseudosymmetric capsids, many larger capsids are constructed by combining pseudosymmetry with quasisymmetry. Analogously, whereas GI_4-F7 and the assemblies reported in the accompanying manuscript[56] are pseudosymmetric, with each distinct subunit in a single chemical environment, GI_9-F7 and its larger counterparts are also quasisymmetric, with genetically identical subunits in more than one chemical environment. The A subunit occupies an asymmetric position in the pentasymmetron and either an asymmetric position in the disymmetron (for even T numbers) or both asymmetric and two-fold symmetric positions in disymmetrons (for odd T numbers greater than nine). Similarly, the B and C subunits occupy different chemical environments depending on their locations in the assembly. Quasisymmetry is enabled by the use of two-component heterotrimers (ABB and AAB), which provides for economy in coding for larger assemblies. The T = 4 structure requires only 3 distinct chains, compared with 4 chains for the more conceptually straightforward approach of a strictly pseudosymmetric ABC heterotrimer and DDD homotrimer. For larger particles the economy is even greater: for example, only 3 unique chains are required to make T = 9 nanocages, but 7 would be needed for the strictly pseudosymmetric approach. The trade-off to this economy is a reduction in precision compared with the approach described in the accompanying Article[56], although as we have shown, this can be partially overcome by modulating the stoichiometry of the assembly reaction.

We used a hierarchical design strategy to fulfil the requirement for multiple designed interfaces in our pseudosymmetric nanomaterials. After first constructing pseudosymmetric heterotrimers and combining these with an existing designed interface to generate pentasymmetrons, producing 240-subunit and larger pseudosymmetric assemblies required only one additional dock-and-design step. Similar hierarchical and modular design strategies are widespread in reticular chemistry[57] and DNA nanotechnology[58], and should become increasingly powerful in protein nanomaterials design as the number and kinds of modular protein building blocks continue to increase[59].

Online content

Any methods, additional references, Nature Portfolio reporting summaries, source data, extended data, supplementary information, acknowledgements, peer review information; details of author contributions and competing interests; and statements of data and code availability are available at https://doi.org/10.1038/s41586-024-08360-6.

1. Alberts, B. The cell as a collection of protein machines: preparing the next generation of molecular biologists. *Cell* **92**, 291–294 (1998).
2. Goodsell, D. S. & Olson, A. J. Structural symmetry and protein function. *Annu. Rev. Biophys. Biomol. Struct.* **29**, 105–153 (2000).
3. King, N. P. & Lai, Y.-T. Practical approaches to designing novel protein assemblies. *Curr. Opin. Struct. Biol.* **23**, 632–638 (2013).
4. Douglas, T. & Young, M. Viruses: making friends with old foes. *Science* **312**, 873–875 (2006).
5. Howorka, S. Rationally engineering natural protein assemblies in nanobiotechnology. *Curr. Opin. Biotechnol.* **22**, 485–491 (2011).
6. Lee, E. J., Lee, N. K. & Kim, I.-S. Bioengineered protein-based nanocage for drug delivery. *Adv. Drug Deliv. Rev.* **106**, 157–171 (2016).
7. López-Sagaseta, J., Malito, E., Rappuoli, R. & Bottomley, M. J. Self-assembling protein nanoparticles in the design of vaccines. *Comput. Struct. Biotechnol. J.* **14**, 58–68 (2016).
8. Huang, P.-S., Boyken, S. E. & Baker, D. The coming of age of de novo protein design. *Nature* **537**, 320–327 (2016).
9. Zhu, J. et al. Protein assembly by design. *Chem. Rev.* **121**, 13701–13796 (2021).
10. King, N. P. et al. Computational design of self-assembling protein nanomaterials with atomic level accuracy. *Science* **336**, 1171–1174 (2012).
11. Bale, J. B. et al. Accurate design of megadalton-scale two-component icosahedral protein complexes. *Science* **353**, 389–394 (2016).
12. de Haas, R. J. et al. Rapid and automated design of two-component protein nanomaterials using ProteinMPNN. *Proc. Natl Acad. Sci. USA* **121**, e2314646121 (2024).
13. Meador, K. et al. A suite of designed protein cages using machine learning and protein fragment-based protocols. *Structure* **32**, 751–765.e11 (2024).
14. Hsia, Y. et al. Design of a hyperstable 60-subunit protein icosahedron. *Nature* **535**, 136–139 (2016).
15. Fletcher, J. M. et al. Self-assembling cages from coiled-coil peptide modules. *Science* **340**, 595–599 (2013).
16. Kobayashi, N. et al. Self-assembling nano-architectures created from a protein nano-building block using an intermolecularly folded dimeric de novo protein. *J. Am. Chem. Soc.* **137**, 11285–11293 (2015).
17. Sciore, A. et al. Flexible, symmetry-directed approach to assembling protein cages. *Proc. Natl Acad. Sci. USA* **113**, 8681–8686 (2016).
18. Lai, Y.-T. et al. Structure of a designed protein cage that self-assembles into a highly porous cube. *Nat. Chem.* **6**, 1065–1071 (2014).
19. Sinclair, J. C., Davies, K. M., Vénien-Bryan, C. & Noble, M. E. M. Generation of protein lattices by fusing proteins with matching rotational symmetry. *Nat. Nanotechnol.* **6**, 558–562 (2011).
20. Malay, A. D. et al. An ultra-stable gold-coordinated protein cage displaying reversible assembly. *Nature* **569**, 438–442 (2019).
21. Cristie-David, A. S. & Marsh, E. N. G. Metal-dependent assembly of a protein nano-cage. *Protein Sci.* **28**, 1620–1629 (2019).
22. Golub, E. et al. Constructing protein polyhedra via orthogonal chemical interactions. *Nature* **578**, 172–176 (2020).
23. Tetter, S. et al. Evolution of a virus-like architecture and packaging mechanism in a repurposed bacterial protein. *Science* **372**, 1220–1224 (2021).
24. Terasaka, N., Azuma, Y. & Hilvert, D. Laboratory evolution of virus-like nucleocapsids from nonviral protein cages. *Proc. Natl Acad. Sci. USA* **115**, 5432–5437 (2018).
25. Butterfield, G. L. et al. Evolution of a designed protein assembly encapsulating its own RNA genome. *Nature* **552**, 415–420 (2017).
26. Edwardson, T. G. W., Tetter, S. & Hilvert, D. Two-tier supramolecular encapsulation of small molecules in a protein cage. *Nat. Commun.* **11**, 5410 (2020).
27. Divine, R. et al. Designed proteins assemble antibodies into modular nanocages. *Science* **372**, eabd9994 (2021).
28. Mohan, K. et al. Topological control of cytokine receptor signaling induces differential effects in hematopoiesis. *Science* **364**, 6442 (2019).

29. Liu, Y., Gonen, S., Gonen, T. & Yeates, T. O. Near-atomic cryo-EM imaging of a small protein displayed on a designed scaffolding system. *Proc. Natl Acad. Sci. USA* **115**, 3362–3367 (2018).
30. McConnell, S. A. et al. Designed protein cages as scaffolds for building multienzyme materials. *ACS Synth. Biol.* **9**, 381–391 (2020).
31. Brouwer, P. J. M. et al. Enhancing and shaping the immunogenicity of native-like HIV-1 envelope trimers with a two-component protein nanoparticle. *Nat. Commun.* **10**, 4272 (2019).
32. Ueda, G. et al. Tailored design of protein nanoparticle scaffolds for multivalent presentation of viral glycoprotein antigens. *eLife* **9**, e57659 (2020).
33. Bruun, T. U. J., Andersson, A.-M. C., Draper, S. J. & Howarth, M. Engineering a rugged nanoscaffold to enhance plug-and-display vaccination. *ACS Nano* **12**, 8855–8866 (2018).
34. Boyoglu-Barnum, S. et al. Quadrivalent influenza nanoparticle vaccines induce broad protection. *Nature* **592**, 623–628 (2021).
35. Marcandalli, J. et al. Induction of potent neutralizing antibody responses by a designed protein nanoparticle vaccine for respiratory syncytial virus. *Cell* **176**, 1420–1431.e17 (2019).
36. Walls, A. C. et al. Elicitation of potent neutralizing antibody responses by designed protein nanoparticle vaccines for SARS-CoV-2. *Cell* **183**, 1367–1382.e17 (2020).
37. Song, J. Y. et al. Safety and immunogenicity of a SARS-CoV-2 recombinant protein nanoparticle vaccine (GBP510) adjuvanted with AS03: A randomised, placebo-controlled, observer-blinded phase 1/2 trial. *eClinicalMedicine* **51**, 101569 (2022).
38. Padilla, J. E., Colovos, C. & Yeates, T. O. Nanohedra: using symmetry to design self assembling protein cages, layers, crystals, and filaments. *Proc. Natl Acad. Sci. USA* **98**, 2217–2221 (2001).
39. Laniado, J. & Yeates, T. O. A complete rule set for designing symmetry combination materials from protein molecules. *Proc. Natl Acad. Sci. USA* **117**, 31817–31823 (2020).
40. Lindstedt, S. & Nishikawa, K. Huxleys' missing filament: form and function of titin in vertebrate striated muscle. *Annu. Rev. Physiol.* **79**, 145–166 (2017).
41. Cramer, P. et al. Structure of eukaryotic RNA polymerases. *Annu. Rev. Biophys.* **37**, 337–352 (2008).
42. Caspar, D. L. D. & Klug, A. Physical principles in the construction of regular viruses. *Cold Spring Harb. Symp. Quant. Biol.* **27**, 1–24 (1962).
43. Harrison, S. C. The familiar and the unexpected in structures of icosahedral viruses. *Curr. Opin. Struct. Biol.* **11**, 195–199 (2001).
44. De Colibus, L. et al. Assembly of complex viruses exemplified by a halophilic euryarchaeal virus. *Nat. Commun.* **10**, 1456 (2019).
45. Liu, H. et al. Atomic structure of human adenovirus by cryo-EM reveals interactions among protein networks. *Science* **329**, 1038–1043 (2010).
46. Veesler, D. et al. Atomic structure of the 75 MDa extremophile *Sulfolobus* turreted icosahedral virus determined by CryoEM and X-ray crystallography. *Proc. Natl Acad. Sci. USA* **110**, 5504–5509 (2013).
47. Fullerton, S. W. B. et al. Mechanism of the class I KDPG aldolase. *Bioorg. Med. Chem.* **14**, 3002–3010 (2006).
48. Ovchinnikov, S., Kamisetty, H. & Baker, D. Robust and accurate prediction of residue-residue interactions across protein interfaces using evolutionary information. *eLife* **2014**, e02030 (2014).
49. Kamisetty, H., Ovchinnikov, S. & Baker, D. Assessing the utility of coevolution-based residue-residue contact predictions in a sequence- and structure-rich era. *Proc. Natl Acad. Sci.* **110**, 15674–15679 (2013).
50. Klinke, S. et al. Structural and kinetic properties of lumazine synthase isoenzymes in the order *Rhizobiales*. *J. Mol. Biol.* **373**, 664–680 (2007).
51. Goldberg, M. A class of multi-symmetric polyhedra. *Tohoku Math. J.* **43**, 104–108 (1937).
52. Zakeri, B. et al. Peptide tag forming a rapid covalent bond to a protein, through engineering a bacterial adhesin. *Proc. Natl Acad. Sci. USA* **109**, E690–E697 (2012).
53. Adachi, K. et al. 37. Capacity of viral genome packaging and internal volumes of AAV viral particles. *Mol. Ther.* **23**, S17 (2015).
54. Lai, Y.-T., Cascio, D. & Yeates, T. O. Structure of a 16-nm cage designed by using protein oligomers. *Science* **336**, 1129 (2012).
55. Bloom, J. D., Labthavikul, S. T., Otey, C. R. & Arnold, F. H. Protein stability promotes evolvability. *Proc. Natl Acad. Sci. USA* **103**, 5869–5874 (2006).
56. Lee, S. et al. Four-component protein nanocages designed by programmed symmetry breaking. *Nature* https://doi.org/10.1038/s41586-024-07814-1 (2024).
57. Furukawa, H., Cordova, K. E., O'Keeffe, M. & Yaghi, O. M. The chemistry and applications of metal-organic frameworks. *Science* **341**, 1230444 (2013).
58. Wagenbauer, K. F., Sigl, C. & Dietz, H. Gigadalton-scale shape-programmable DNA assemblies. *Nature* **552**, 78–83 (2017).
59. Watson, J. L. et al. De novo design of protein structure and function with RFdiffusion. *Nature* **620**, 1089–1100 (2023).
60. Brouwer, P. J. M. et al. Two-component spike nanoparticle vaccine protects macaques from SARS-CoV-2 infection. *Cell* **184**, 1188–1200.e19 (2021).

Methods

Pseudosymmetric trimer design

To identify mutations for altering trimer assembly specificity, we first identified all pairs of interacting residues in the trimer interface. Contacts were defined as any residue with a heavy (that is, non-hydrogen) atom within 4 Å of a heavy atom in a residue across the interface. We then used Rosetta to calculate the total score of poses containing all possible pairs of mutations, as well as the difference in score between the trimeric and monomeric states using the ddG filter. Example scripts are provided as supplementary files. Individual mutations were evaluated by comparing their ddG and total scores to those of the wild-type (WT) interface according to equation (1). The total scores and ddG values of the paired mutations were similarly normalized according to equation (2).

$$\begin{aligned}&\text{Single mutant } \Delta\text{score} = \text{score}_{\text{mutant}} - \text{score}_{\text{WT}};\\&\text{Single mutant } \Delta\text{ddG} = \text{ddG}_{\text{mutant}} - \text{ddG}_{\text{WT}}\end{aligned} \quad (1)$$

$$\begin{aligned}&\text{Double mutant } \Delta\text{score} = \text{score}_{\text{mutant}} - \text{score}_{\text{WT}};\\&\text{Double mutant } \Delta\text{ddG} = \text{ddG}_{\text{mutant}} - \text{ddG}_{\text{WT}}\end{aligned} \quad (2)$$

Ideal mutant pairs were those where one or both single mutations increased the energy of the trimer relative to the wild type (that is, normalized scores > 0) while the double mutation had no effect or stabilized the trimer (that is, normalized scores ≤ 0). We also identified likely positions for design using coevolutionary analysis[48,49]. Strongly co-evolving residues at the protein–protein interface were identified using GREMLIN. We then identified mutations that were negatively correlated with the wild-type pair for testing experimentally.

Mutant protein expression

Mutant I53-50A trimers were expressed at three scales. Small-scale expression was performed at 1 ml culture volume in 96-well plates with 2 ml well volume. Medium-scale expressions were performed at 50 ml culture volume in 250 ml baffled shake flasks. Large-scale expressions were performed at 500 ml culture volumes in 2 l baffled shake flasks. All proteins were expressed in T7 competent *E. coli* in TB medium, with IPTG induction for 3 h at 37 °C. Cells were pelleted and frozen at −20 °C until lysis. Prior to lysis cells were defrosted on ice in lysis buffer (50 mM Tris pH 8.0, 250 mM NaCl, 20 mM imidazole, 1 mM phenylmethylsulfonyl fluoride, 1 mM dithiothreitol (DTT), 0.1 mg ml^{-1} DNase, and 0.1 µM RNase, unless otherwise noted). Small-scale expressions were lysed with a plate sonicator (QSonica), medium-scale expressions were lysed with a probe sonicator, and large-scale expressions were lysed by microfluidization (18,000 psi, one pass). Lysates from small-scale expressions were clarified by centrifugation in a swinging bucket rotor at 4,000*g*. Lysates from medium- and large-scale expression lysates were clarified by centrifugation at 12,000*g* in a fixed-angle rotor.

I53-50B expression and purification

Pentameric I53-50B was produced recombinantly in *E. coli*. A pET29b expression plasmid encoding I53-50B.4PT1[11] was synthesized by GenScript using the NdeI and XhoI restriction sites with a double stop codon just before the C-terminal polyhistidine tag. Tagless protein was expressed in Lemo21(DE3) cells (NEB) in LB (10 g Tryptone, 5 g Yeast Extract, 10 g NaCl) grown in a 10 l BioFlo 320 Fermenter (Eppendorf). At inoculation, impeller speed was set to 225 rpm, gas flow rate was set to 5 standard litres per minute with O_2 supplementation as part of the dissolved-oxygen aeration cascade, and the temperature set to 37 °C. At the onset of a dissolved oxygen spike (OD ~ 12), the culture was fed with a bolus addition of 100 ml of 100% glycerol and induced with 1 mM IPTG. During this time, the culture temperature was reduced to 18 °C and O_2 supplementation was ceased, with expression continuing until OD reached ~20. The culture was collected by centrifugation and the protein was purified from inclusion bodies. First, pellets were resuspended in PBS, homogenized, and then lysed by microfluidization using a Microfluidics M110P at 18,000 psi. Following sample clarification by centrifugation (24,000*g* for 30 min), the supernatant was discarded and protein was extracted from the pellet using a series of three washes. The first wash consisted of PBS, 0.1% Triton X-100, pH 8.0. The second wash consisted of PBS, 1 M NaCl, pH 8.0, and the final wash (extraction) consisted of PBS, 2 M urea, 0.75% CHAPS (3-[(3-cholamidopropyl)dimethylammonio]-1-propanesulfonate), pH 8.0. Following extraction, the sample was applied to a DEAE Sepharose FF column (Cytiva) on an AKTA Avant150 FPLC system (Cytiva). After sample binding, the column was washed with 5 column volumes of PBS at pH 8.0 with 0.1% Triton X-100, followed by a wash with 5 column volumes of PBS at pH 8.0 with 0.75% CHAPS. The protein was eluted with 3 column volumes of PBS at pH 8.0 with 500 mM NaCl. After purification, fractions were pooled and concentrated in 10K MWCO centrifugal filters (Millipore), sterile filtered (0.22 µm), aliquoted and flash-frozen in liquid nitrogen, and stored at −80 °C until use.

Assembly competency analysis

Single mutations were introduced into the I53-50A trimer[11] by QuikChange site-directed mutagenesis. Sequence-verified mutants were expressed at small scale. Clarified lysates were separated from pellets and a 5 µl aliquot was set aside for characterization by SDS–PAGE. The pellet was resuspended in lysis buffer and a 5 µl aliquot was set aside for characterization by SDS–PAGE. Clarified lysate was immediately mixed with purified I53-50B.4PT1 pentamer. Because trimer expression levels varied from mutant to mutant, pentamer was added at three different concentrations. To 10 µl lysate, 7.5, 2.5 or 0 µl lysis buffer was added, followed by 2.5, 7.5 or 10 µl I53-50B.4PT1 pentamer at 1.8 mg ml^{-1}. The assembly reaction was allowed to proceed for 30 min at room temperature. Purified I53-50B.4PT1 pentamer was included on all native PAGE gels. A 10 µl aliquot of each assembly reaction was mixed 1:1 with Native Sample Buffer (Bio-Rad Laboratories), loaded into precast 4–15% polyacrylamide gels (Bio-Rad Laboratories), and run with 1× Tris-Glycine Native PAGE buffer for 3 h at 200 V. The gel was stained with GelCode Blue (Thermo Fisher Scientific) and destained in water. The lack of an I53-50 nanocage band on the native gel indicated single mutations that disrupted either trimer formation or trimer geometry such that the mutant trimer was no longer assembly-competent.

Screening of mutant combinations

Single mutants that disrupted I53-50A trimer—and therefore I53-50 nanocage—formation were combined with 'rescue' mutations intended to generate pseudosymmetric I53-50A trimers. Synthetic DNA encoding potential combinations were ordered as heterotrimeric operons cloned into pCDB179 from IDT. To facilitate detection of the distinct components of the heterotrimer, a 6×His-SUMO domain was added to one subunit and sfGFP and an avi-tag added to a second subunit via genetic fusion. The third subunit bore a Strep-tag via genetic fusion. Variants were tested for I53-50 nanocage formation using trimer-containing *E. coli* lysates and purified I53-50B pentamer as described above. Combinations that formed I53-50 nanocages were expressed at large scale and purified by Ni^{2+} affinity chromatography on a HisTrap FF column (Cytiva). In brief, clarified lysate was passed through a pre-equilibrated 5 ml HisTrap FF column, washed with 3–5 column volumes of wash buffer (50 mM Tris pH 8.0, 250 mM NaCl, 20 mM imidazole, 1 mM DTT), and heterotrimer was eluted with either a step elution or a gradient over 40 min at 3 ml min^{-1} flow rate into 100% elution buffer (50 mM Tris pH 8.0, 250 mM NaCl, 500 mM imidazole, 1 mM DTT). Major fractions corresponding to the two observed peaks in the elution profile were pooled separately, concentrated in a 30-kDa

cut-off Amicon concentrator (Millipore), and injected onto a pre-equilibrated Superdex 200 Increase 10/300 column (Cytiva). The SEC buffer was 25 mM Tris pH 8.0, 150 mM NaCl, 1 mM DTT. Fractions corresponding to the trimer peak from each chromatogram were collected for analysis by native mass spectrometry. Alternatively, the IMAC eluate was pooled and loaded onto a StrepTrap HP column (Cytiva) pre-equilibrated in binding buffer (100 mM Tris pH 8.0, 150 mM NaCl, 1 mM EDTA, and 1 mM DTT). The column was then washed with 10 column volumes of binding buffer, or until the A280 absorbance leveled off at baseline and eluted with a step elution in binding buffer plus 2.5 mM desthiobiotin. Major fractions were analysed by reducing SDS–PAGE.

Native mass spectrometry

Trimer purity, identity, and oligomeric state were analysed by on-line buffer-exchange mass spectrometry[61] in 200 mM ammonium acetate using a Vanish ultra-performance liquid chromatography coupled to a Q Exactive ultra-high mass range Orbitrap mass spectrometer (Thermo Fisher Scientific). The recorded mass spectra were deconvolved with UniDec version 4.2+ (ref. 62).

Assembly of I53-50 nanocages using pseudosymmetric I53-50A heterotrimers

The native mass spectrometry-verified pseudosymmetric I53-50A heterotrimer was expressed and purified at medium scale as described above and mixed at a 1:1 molar ratio with purified I53-50B.4PT1 pentamer and allowed to assemble at room temperature for 30 min. Assembled nanocages were characterized by DLS and negative-stain electron microscopy as described below.

Computational design of T = 4 nanocages

We created a model of the pentasymmetron by extracting five trimers surrounding the icosahedral five-fold from I3-01[14]. We reverted the interface residues on the unpaired subunit back to the original 1WA3 sequence, mutated 12 residues to negatively charged amino acids to enhance expression and facilitate purification, then combined each trimer into a single chain so that the pentasymmetron could be treated computationally as a simple homopentamer. We used previously described protocols[11] to dock and design T = 4 nanocages, with some modifications to the design script. Example design scripts are provided as supplementary files. Docked configurations were manually screened to ensure interfaces were between the unpaired pentasymmetron subunit and the homotrimer. Designs were visually inspected and any overly exposed hydrophobic residues introduced during design were reverted to their wild-type identities.

Screening of T = 4 nanocages by co-purification

Three tricistronic genes were ordered from IDT. An N-terminal GFP was included on the A subunit of the pentasymmetron heterotrimer as a mass tag. A C-terminal 6×His tag was added to the C subunit. Genes were expressed at medium scale. Clarified lysate was loaded onto 1 ml of Ni-NTA resin (Thermo Fisher Scientific) pre-equilibrated in wash buffer. After washing with three column volumes of wash buffer, the protein was eluted with two column volumes of elution buffer. Eluate was screened for the presence of all three gene products by SDS–PAGE.

Purification of co-expressed GI_4-F7

GI_4-F7 nanocages expressed tricistronically at large scale were purified by loading on a 5 ml HisTrap FF column (Cytiva) equilibrated in wash buffer (50 mM Tris pH 8.0, 250 mM NaCl, 20 mM imidazole, 1 mM DTT). After loading, the column was washed with 3–5 column volumes of wash buffer and protein was eluted with a gradient into 100% elution buffer (50 mM Tris pH 8.0, 250 mM NaCl, 500 mM imidazole, 1 mM DTT) over 40 min at 3 ml min^{-1}. The major fractions from elution were pooled, concentrated to ~1 ml, and loaded onto an equilibrated Sephacryl S-500 HR 10/300 GL. SEC buffer was 25 mM Tris pH 8.0, 150 mM NaCl, 1 mM DTT.

Purification of GI_4-F7 heterotrimeric and homotrimeric components

For in vitro assembly, the heterotrimeric component of GI_4-F7, comprising only the A and B chains, was expressed bicistronically. The A chain was modified with an N-terminal 6×His tag. When expressed this way, some AAA nanocages and BBB homotrimers probably assemble in addition to AAB and ABB heterotrimers. To purify AAB from ABB heterotrimers, the bicistronic gene was expressed at large scale with the modification that 0.75% CHAPS was added to the lysis buffer and DTT was omitted. Clarified lysate was purified with a 5 ml HisTrap FF column as described above. Elution chromatograms contained three peaks. The first peak was predominantly the ABB heterotrimer, the second peak was predominantly AAB heterotrimer, and the third peak was predominantly AAA homotrimers assembled into an I3-01-like particle. Any BBB homotrimer would be in the flow-through. The first and second peaks were pooled separately and concentrated to ~1 ml. To remove any residual I3-01-like nanocage, we further purified the concentrated fractions on a Superose 6 Increase 10/300 column. The SEC buffer was 25 mM Tris pH 8.0, 150 mM NaCl, 0.75% w/v CHAPS. Glycerol was added to purified heterotrimer to a final concentration of 5%, the concentration was determined by A280, and 1 ml aliquots were flash-frozen in liquid nitrogen. Aliquots were stored at −80 °C until use. The homotrimer components were expressed at large scale and purified by IMAC in the same way as the co-expressed GI_4-F7 nanocages except that 1% CHAPS was added to all buffers. It was further purified by SEC on a HiLoad 26/600 Superdex 200 PG column in 25 mM Tris pH 8.0, 150 mM NaCl, 5% glycerol, 1.0% w/v CHAPS, 1 mM DTT. The total trimer protein concentration was measured by A280, flash-frozen in liquid nitrogen in 1 ml aliquots, and stored at −80 °C until use.

In vitro assembly of GI_T-F7 nanocages

To assemble GI_T-F7 nanocages, components were mixed at various stoichiometries depending on the target assembly state in the presence of 3% CHAPS, a condition that prevented premature assembly. This was necessary to prevent the assembly of off-target species during addition of the multiple components required to generate the target assemblies. For example, mixing BBB–CCC heterotrimers prior to the addition of AAB and ABB components under assembly-permissive conditions would result in 2D arrays instead of GI_T-F7 nanocages (see Extended Data Fig. 6). Once all components were added, the mixtures were dialysed into 0% CHAPS overnight at room temperature in a 30-kDa cut-off dialysis cassette. As an extra precaution, the AAB and ABB heterotrimers were mixed first since they do not directly interact with the BBB homotrimer, followed by addition of the CCC homotrimer. Nanocages were prepared fresh for each experiment, or stored at 4 °C for up to three days. To assemble BBB–CCC 2D arrays, the components were first individually dialysed to remove CHAPS, and then mixed at a 1:1 stoichiometric ratio and allowed to assemble overnight at room temperature.

Characterization of assemblies

Assemblies were characterized in solution by DLS. Samples were measured in triplicate, technical replicates, using an UNcle (UNchained Labs) according to the manufacturer's directions. In brief, 8.8 µl of sample was loaded in triplicate into the capillary cassette. For each replicate, 10 acquisitions 10 s in length were collected. Assemblies were further characterized by negative-stain electron microscopy. Samples were diluted to between 0.1 and 0.5 mg ml^{-1} total protein depending on the assembly stoichiometry, applied to a glow-discharged thick carbon film 400 mesh copper grid (Electron Microscopy Sciences), and stained with 2% uranyl formate. Care was taken to ensure the stain thickness

was sufficient to support the larger assemblies. Micrographs were collected on a Talos L120C (FEI) at up to 48,000× magnification. Individual micrographs were processed with ImageJ.

Conjugation of RBD antigens to GI_T-F7 nanocages and characterization by negative-stain electron microscopy

To enable conjugation of antigens to assembled nanocages, CCC trimers were fused to a SpyCatcher002 motif at their C terminus, expressed in *E. coli*, and purified via IMAC and SEC, as described above. Nanocages were then assembled at the appropriate stoichiometries for T = 4 and T = 9 assemblies by dialysing into a 0% CHAPS solution overnight. Assembled particles were then mixed with an excess of RBD-SpyTag002 and mixed at 4 °C for 3 h. Conjugation was confirmed by SDS–PAGE, wherein the mass of RBD showed a ~30 kDa increase, consistent with conjugation to CCC proteins in nanocage assemblies. After conjugation, particles were also visualized by negative-stain electron microscopy to confirm intact assemblies. Samples were prepared by applying 3 µl of a 5 µM nanocage solution to glow-discharge carbon-coated grids, followed by staining with uranyl formate 3 times prior to imaging. EPU software (Thermo Fisher) was used to collect at least 100 micrographs of each sample. Images were imported to CryoSparc and particles were averaged to obtain initial 2D classes. Selected classes were then used to generate templates for a second round of particle picking, and new particles were averaged multiple times to obtain the 2D classes shown in Fig. 3i.

B cell activation assay

The COVA2-15 IgG RAMOS cell line was generously provided by the van Gils laboratory[60] and not authenticated further. For Ca^{2+} flux experiments, cells were loaded with FuraRed cell-permeable dye (Thermo Fisher) for 30 min in RPMI1640 supplemented with 10% fetal clone II, 1% L-glutamax, and 1% penicillin–streptomycin (complete medium) at a cell concentration of 1×10^7 per ml. Cells were then washed with 10× volume complete medium, resuspended at 2×10^6 cells per ml in complete medium, and aliquoted at 0.25 ml into individual FACS tubes. Samples were kept at room temperature and then warmed in a 37 °C bath for 3 min immediately before use. Acquisition was performed on an Attune CytPix flow cytometer (Thermo Fisher) with baselines recorded for 30 s for each sample before addition of antigen and measurement of BCR-specific activation. For gating strategy, see Supplementary Fig. 6. A polyclonal goat anti-human IgG F(ab')2 (Southern Biotech) was used as a positive control for signalling resulting from IgG BCR cross-linking by addition of 2.5 µg to cells. The FuraRed ratio of bound (fluorescence in VL3) and unbound (fluorescence in BL1) Ca^{2+} was used for analysis using FlowJo v10 (BD Biosciences). Cell lines were not tested for mycoplasma.

Cryo-EM sample preparation, data collection and data processing

Three microlitres of 3 mg ml^{-1} GI_4-F7, GI_9-F7, and GI_{16}-F16 were loaded onto freshly glow-discharged R 2/2 UltrAuFoil grids, prior to plunge freezing using a Vitrobot Mark IV (Thermo Fisher Scientific) with a blot force of 0 and 6 sec blot time at 100% humidity and 22 °C. Data were acquired using an FEI Titan Krios transmission electron microscope operated at 300 kV and equipped with a Gatan K3 direct detector and Gatan Quantum GIF energy filter, operated in zero-loss mode with a slit width of 20 eV. For GI_4-F7 and GI_9-F7, automated data collection was carried out using Leginon[63] at a nominal magnification of 105,000× with a pixel size of 0.843 Å. 7,249 and 2,558 micrographs were collected with a defocus range comprised between −0.5 and −2.5 µm, respectively. The dose rate was adjusted to 15 counts per pixel per s, and each movie was acquired in super-resolution mode fractionated in 75 frames of 40 ms. For the GI_{16}-F7 data set, automated data collection was carried out using Leginon[63] at a nominal magnification of 64,000× with a pixel size of 1.42 Å. In total, 2,268 micrographs were collected with a defocus range between −0.5 and −3.5 µm. The dose rate was adjusted to 15 counts per pixel per s, and each movie was acquired in super-resolution mode fractionated in 50 frames of 100 ms. Movie frame alignment, estimation of the microscope contrast-transfer function parameters, particle picking and extraction were carried out using Warp[64].

Two rounds of reference-free 2D classification were performed using CryoSPARC[65] to select well-defined particle images. These selected particles were subjected to two rounds of 3D classification with 50 iterations each (angular sampling 7.5° for 25 iterations and 1.8° with local search for 25 iterations) using Relion[66] with an initial model generated with ab initio reconstruction in cryoSPARC. 3D refinements were carried out using non-uniform refinement along with per-particle defocus refinement in CryoSPARC. Selected particle images were subjected to the Bayesian polishing procedure[67] implemented in Relion 3.1 before performing another round of non-uniform refinement in cryoSPARC followed by per-particle defocus refinement and again non-uniform refinement. To further improve the density of the asu, the particles were symmetry-expanded and subjected to focus 3D classification without refining angles and shifts. Particles belonging to classes with the best resolved asu density were selected and then subjected to local refinement using CryoSPARC. Local resolution estimation,and sharpening were carried out using CryoSPARC. Reported resolutions are based on the gold-standard Fourier shell correlation of 0.143 criterion and Fourier shell correlation curves were corrected for the effects of soft masking by high-resolution noise substitution[68,69].

Model building and refinement

UCSF Chimera[70] and Coot[71] were used to fit atomic models into the cryo-EM maps. GI_4-F7 and GI_9-F7 asu models were refined and relaxed using Rosetta using sharpened and unsharpened maps[72,73]. For GI_4-F7 or GI_9-F7 icosahedral model, all of the side chains of GI_4-F7 or GI_9-F7 asu model are truncated except Gly, Cys, and Pro residues and the symmetry-related copies were generated in ChimeraX with cryo-EM maps.

Alignments and images

To align the cryo-EM models to the design model, both models were centred at the origin and their icosahedral symmetry axes aligned in PyMOL[74]. The Cα r.m.s.d. was calculated using the rms_cur function in PyMOL. To measure deviations in the rigid-body degrees of freedom, copies of the pentasymmetron, disymmetron, and trimer (or trimers for GI_9-F7) from the cryo-EM model were aligned to the design model using the 'super' function in PyMOL. We then calculated the rotations and translations from the transformation matrix between the corresponding component of the original cryo-EM model and the aligned cryo-EM model. We applied the same approach to the heterotrimer (and homotrimer for GI_9-F7) components to obtain rotations and translations within the pentasymmetron, disymmetron, and homotrimer components, respectively. We found that the 'super' function in PyMOL was very sensitive to chain and residue numbering, as well as some of the minor differences between the design model and cryo-EM model. Therefore, for all alignments using PyMOL, we made sure to harmonize residue numbering, chain IDs, and remove any residues present in only one model or the other. For that reason, aligned images were generated using the mm command in ChimeraX[75] and verified to ensure that the alignments closely matched those generated on the trimmed models created with the super function in PyMOL.

Scripts and plots

All data were processed and plotted using Python 3.8.8, matplotlib 3.3.4 and seaborn 0.11.1.

Reporting summary

Further information on research design is available in the Nature Portfolio Reporting Summary linked to this article.

Data availability

Electron microscopy maps and models for GI_4-F7 are available from the Electron Microscopy Data Bank (EMD) under accession number EMD-47034, local refinements for GI_4-F7 are available under accession number EMD-47036 and also in the Protein Data Bank (PDB) under accession number 9DND, electron microscopy maps and models for GI_9-F7 are available under accession number EMD-47037, local refinements for GI_9-F7 are available under PDB ID 9DNE and EMD-47038, and electron microscopy maps and models for GI_{16}-F7 are available under accession number EMD-47039. Structural data for the KDPG from *T. maritima*, the lumazine synthase from *Mesorhizobium loti* and I3-01 are available in the Protein Data Bank (PDB IDs 1WA3, 2OBX and 8ED3, respectively). All other data are available in the manuscript or the supplementary materials.

Code availability

Example.xml scripts, command lines, and a README file are available on GitHub at https://github.com/quecloud/Hierarchical-pseudosymmetric-nanocage-design and through Zenodo at https://doi.org/10.5281/zenodo.13958626 (ref. 76).

61. VanAernum, Z. L. et al. Rapid online buffer exchange for screening of proteins, protein complexes and cell lysates by native mass spectrometry. *Nat. Protoc.* **15**, 1132–1157 (2020).
62. Marty, M. T. et al. Bayesian deconvolution of mass and ion mobility spectra: from binary interactions to polydisperse ensembles. *Anal. Chem.* **87**, 4370–4376 (2015).
63. Suloway, C. et al. Automated molecular microscopy: the new Leginon system. *J. Struct. Biol.* **151**, 41–60 (2005).
64. Tegunov, D. & Cramer, P. Real-time cryo-electron microscopy data preprocessing with Warp. *Nat. Methods* **16**, 1146–1152 (2019).
65. Punjani, A., Rubinstein, J. L., Fleet, D. J. & Brubaker, M. A. cryoSPARC: algorithms for rapid unsupervised cryo-EM structure determination. *Nat. Methods* **14**, 290–296 (2017).
66. Zivanov, J. et al. New tools for automated high-resolution cryo-EM structure determination in RELION-3. *eLife* **7**, e42166 (2018).
67. Zivanov, J., Nakane, T. & Scheres, S. H. W. A Bayesian approach to beam-induced motion correction in cryo-EM single-particle analysis. *IUCrJ* **6**, 5–17 (2019).
68. Chen, S. et al. High-resolution noise substitution to measure overfitting and validate resolution in 3D structure determination by single particle electron cryomicroscopy. *Ultramicroscopy* **135**, 24–35 (2013).
69. Rosenthal, P. B. & Henderson, R. Optimal determination of particle orientation, absolute hand, and contrast loss in single-particle electron cryomicroscopy. *J. Mol. Biol.* **333**, 721–745 (2003).
70. Pettersen, E. F. et al. UCSF Chimera—a visualization system for exploratory research and analysis. *J. Comput. Chem.* **25**, 1605–1612 (2004).
71. Emsley, P., Lohkamp, B., Scott, W. G. & Cowtan, K. Features and development of Coot. *Acta Crystallogr. D* **66**, 486–501 (2010).
72. Frenz, B. et al. Automatically fixing errors in glycoprotein structures with Rosetta. *Structure* **27**, 134–139.e3 (2019).
73. Wang, R. Y.-R. et al. Automated structure refinement of macromolecular assemblies from cryo-EM maps using Rosetta. *eLife* **5**, e17219 (2016).
74. The PyMOL Molecular Graphics System, version 1.8 (Schrödinger, 2015).
75. Pettersen, E. F. et al. UCSF ChimeraX: structure visualization for researchers, educators, and developers. *Protein Sci.* **30**, 70–82 (2021).
76. Dowling, Q. quecloud/Hierarchical-pseudosymmetric-nanocage-design: release to support publication (V1.0.1). *Zenodo* https://doi.org/10.5281/zenodo.13958626 (2024).

Acknowledgements The authors thank S. Wrenn and the IPD Nanoparticle Core for assisting with protein production and purification; M. van Gils for COVA2-15 B cells; F. Praetorius and the King laboratory for comments on the manuscript; R. Krishnamurty for programme management; and K. van Wormer and L. Goldschmidt for maintaining laboratory and computational resources at the Institute for Protein Design. Native mass spectrometry measurements were provided by the Wysocki laboratory at the Ohio State University. pCDB179 was a gift from C. Bahl (Addgene plasmid #91960). This work was funded by the Bill & Melinda Gates Foundation (INV-010680 to D.B. and N.P.K.), the National Science Foundation (DMREF 1629214 to D.B. and N.P.K.), the National Institute of Allergy and Infectious Disease (U54AI170856 to N.P.K., 1P01AI167966 to D.V. and N.P.K., DP1AI158186 and 75N93022C00036 to D.V.), the Defense Threat Reduction Agency (HDTRA1-18-1-0001 to D.B. and N.P.K.), generous gifts from the Audacious Project and Open Philanthropy, and the University of Washington Arnold and Mabel Beckman cryo-EM centre and the National Institute of Health grant S10OD032290 (to D.V.). D.V. and D.B. are Investigators of the Howard Hughes Medical Institute. The NIH-funded Resource for Native Mass Spectrometry-Guided Structural Biology at The Ohio State University is funded by NIH P41 GM128577 awarded to V. Wysocki.

Author contributions Q.M.D., Y.H., D.B. and N.P.K. conceived the study. Q.M.D. designed the nanomaterials. Q.M.D. performed bioinformatics analyses. Q.M.D., N.C.G. and A.L.B. produced and experimentally characterized pseudosymmetric mutants. Q.M.D., N.C.G. and R.R. developed purification methods used in this study. C.D.W. developed the 12 negative mutants used to facilitate production of the pentasymmetron. Q.M.D., N.C.G. and R.R. produced and characterized the nanocages. Q.M.D., N.C.G., E.C.Y., A.J.W., Y.H. and N.P.K. determined the geometric principles of assembly. Q.M.D. and C.N.F. produced, characterized and collected negative-stain electron microscopy data of the 2D arrays. C.N.F and A.D. produced and characterized antigen-bearing nanocages. S.O. performed the B cell activation assays. Y.-J.P. collected the cryo-EM data. Y.-J.P. and D.V. analysed and processed the cryo-EM data. All authors analysed data. Q.M.D. and N.P.K. wrote and revised the manuscript with input from all authors.

Competing interests The authors declare no competing interests.

Additional information

Supplementary information The online version contains supplementary material available at https://doi.org/10.1038/s41586-024-08360-6.

Correspondence and requests for materials should be addressed to Neil P. King.

Peer review information *Nature* thanks the anonymous reviewer(s) for their contribution to the peer review of this work.

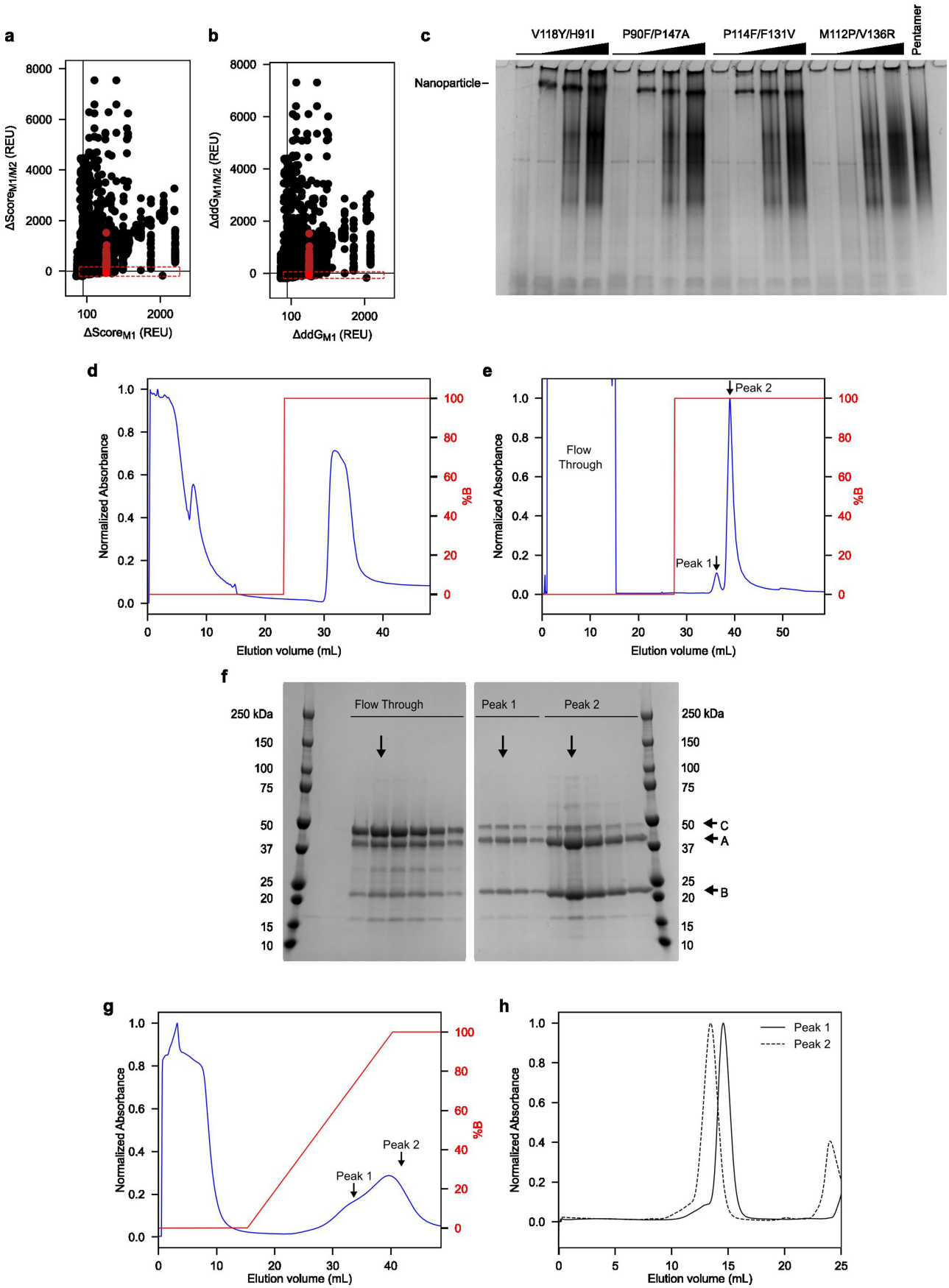

Extended Data Fig. 1 | See next page for caption.

Extended Data Fig. 1 | "ABC" design and purification and characterization of "ABC" tricistronic and "AB" bicistronic constructs. a, ΔddG filter metric. **b**, ΔScore metric. Dark red points correspond to the single mutation P114F. The bright red point corresponds to the double mutant P114F/F131V. The red dotted boxes represent cutoffs used to select mutants for testing. **c**, Recovery of trimer geometry was assayed by assembling double mutant I53-50A trimers in clarified *E. coli* lysates with purified I53-50B pentamer and evaluating the presence or absence of I53-50 nanocages by native PAGE. Black wedges indicate increasing pentamer concentration in each series of assembly reactions. For gel source data, see Supplementary Fig. 2. **d**, The ABC heterotrimer was purified by IMAC with a step elution followed by **e**, StrepTrap purification. The A chain contained a hexa-histidine and SUMO tag, the B chain contained a Strep tag, and the C chain contained sfGFP and avi tags. The eluate of this two-step purification method should therefore only contain trimers that include both the A and B chains. An optimal result would be equimolar amounts of the A, B, and C chains. **f**, SDS-PAGE of the StrepTrap purification revealed that the eluate contained an excess of the A and B chains and less of the C chain. For gel source data, see Supplementary Fig. 3. To test the ability of the A and B chains only to assemble into heterotrimers, we expressed an AB bicistronic gene and **g**, purified the resulting proteins by IMAC with a gradient elution. Two broad and overlapping peaks were observed. The leading half of the first peak and trailing half of the second peak were collected and **h**, further purified by SEC. Peak 2 has a lower retention volume than peak 1, suggesting a difference in molecular weight. These results are consistent with assembly of an ABB heterotrimer (earlier IMAC elution, later SEC elution) and an AAB heterotrimer (later IMAC elution, earlier SEC elution). We confirmed this interpretation by native mass spectrometry (Fig. 1g).

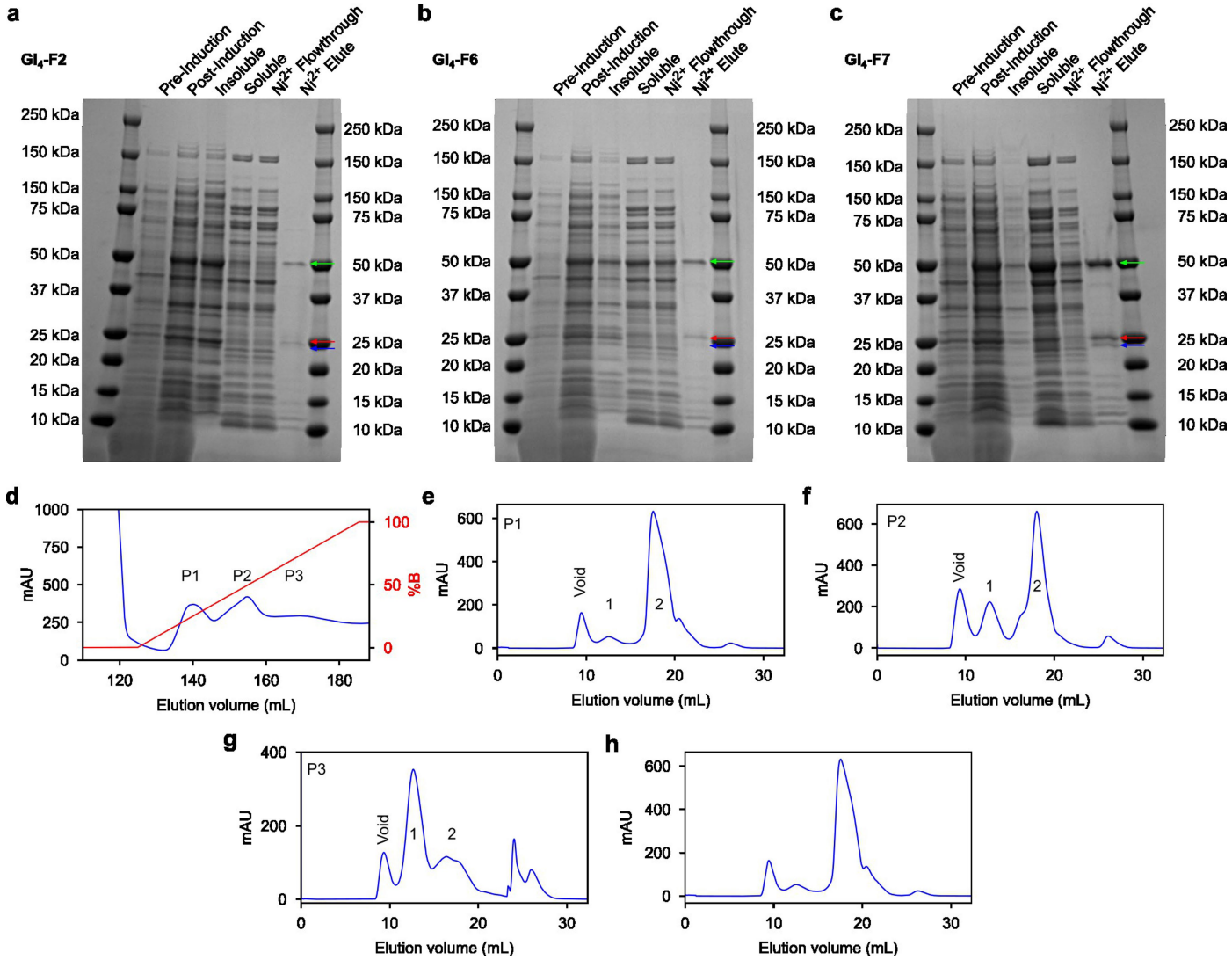

Extended Data Fig. 2 | Screening of GI_4 designs and in vitro assembly of GI_4-F7 from purified components. Expression and screening by SDS-PAGE for GI_4 designs **a**, GI_4-F2, **b**, GI_4-F6 and **c**, GI_4-F7. Bands for chains A (green arrow), B (blue arrow), and C (red) arrow are indicated. The presence of all three bands in the Ni^{2+} Elute lanes of GI_4-F6 and GI_4-F7 indicates interactions between the A, B, and C chains. For gel source data, see Supplementary Fig. 4. **d**, HisTrap elution chromatogram of AB bicistronic expression. Blue, absorbance at 280 nm; red, gradient elution. Peak 1 (P1) is predominantly ABB, P2 is predominantly AAB, and P3 is predominantly the A chain, which assembles into 60-subunit I3-01-like nanocages. **e**, Superdex 200 Increase 10/300 chromatogram of P1 from the HisTrap elution. The first peak following the void volume (1) is predominantly I3-01-like nanocages and (2) is predominantly ABB heterotrimer. **f**, Superdex 200 Increase 10/300 chromatogram of P2 from the HisTrap elution. (1) is predominantly I3-01-like nanocages and (2) is predominantly AAB heterotrimer. **g**, Superdex 200 Increase 10/300 chromatogram of P3 from the HisTrap elution. (1) is predominantly I3-01-like nanocages and (2) is predominantly AAB heterotrimer. **h**, SEC purification of GI_4-F7 on a Sephacryl S-500 HR 10/300 GL column. Peak 1 contains the assembly while peak 2 is residual homotrimer component.

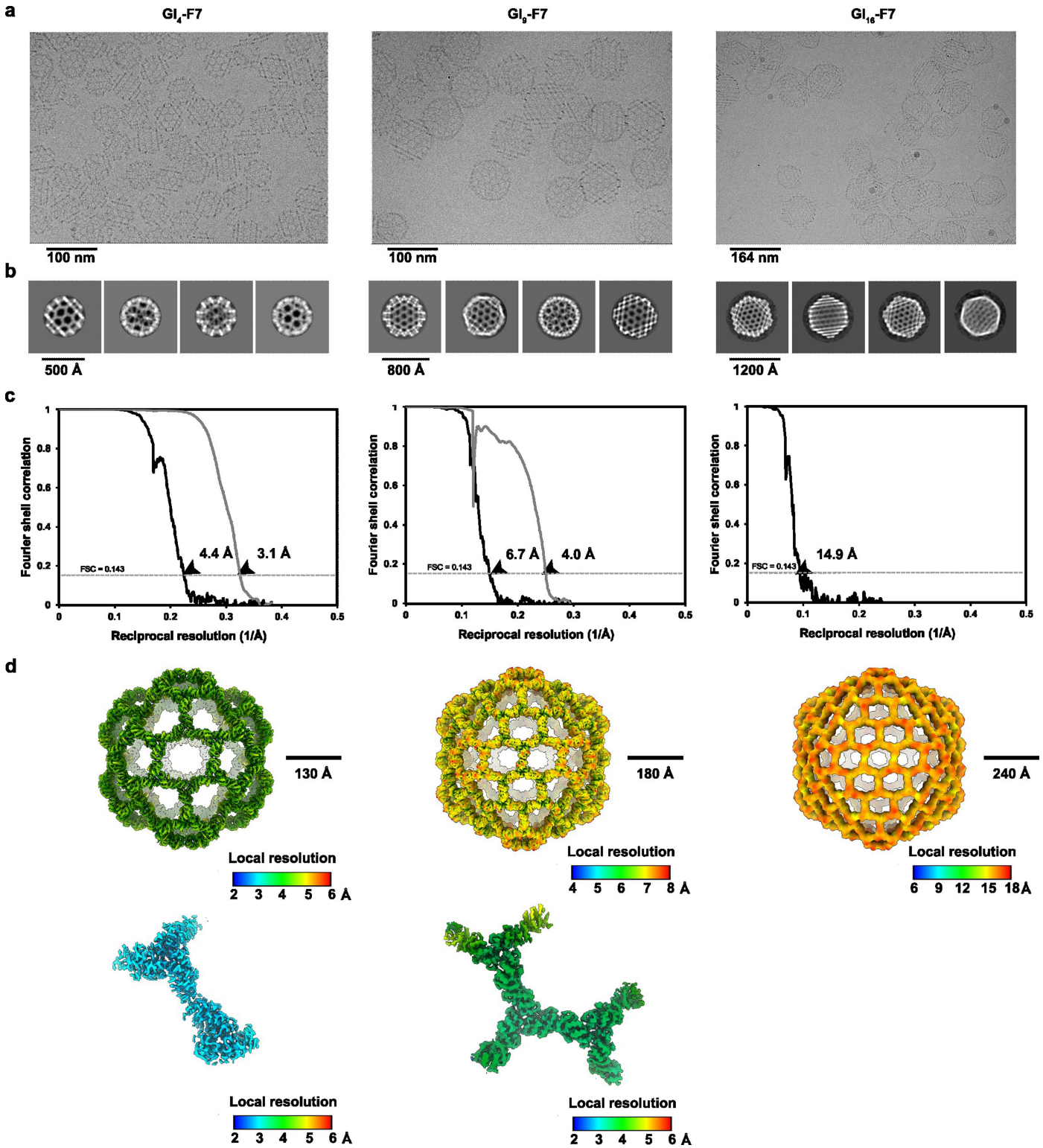

Extended Data Fig. 3 | CryoEM data processing. (**a-b**) Representative electron micrographs **a**, and 2D class averages **b**, of GI_4-F7 (left), GI_9-F7, (middle) and GI_{16}-F7 (right). **c**, Gold-standard Fourier shell correlation curves for the 3D reconstructions of GI_4-F7 (left), GI_9-F7 (middle) and GI_{16}-F7 (right) (black line) and locally refined asus (gray lines). The 0.143 cutoff is indicated by a horizontal dashed line. (**d-e**) Local resolution maps calculated using cryoSPARC for **d**, the 3D reconstructions of GI_4-F7 (left) and locally refined asu (left, bottom), GI_9-F7 (middle) and locally refined asu (middle, bottom), and GI_{16}-F7 (right).

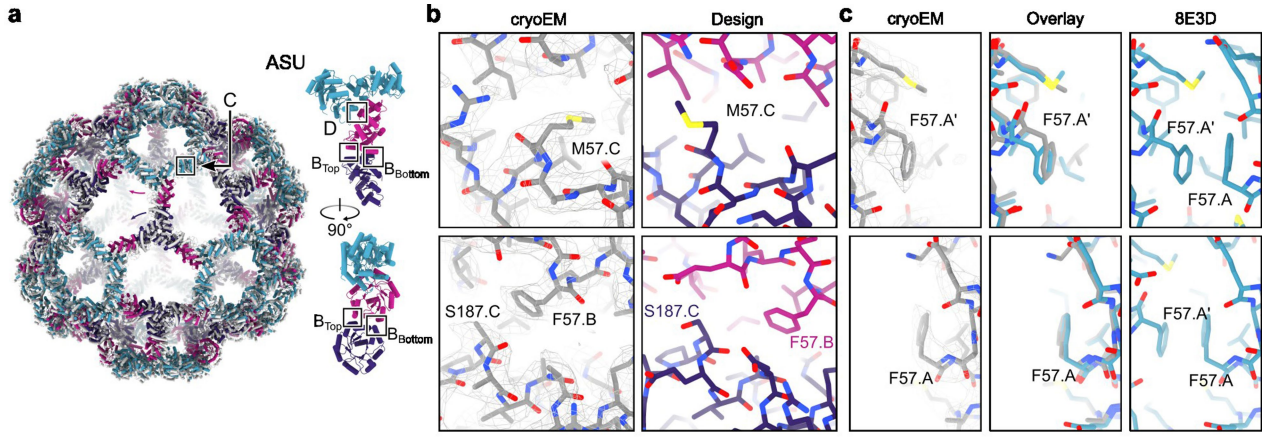

d

Component	Axis	Translation (Å)	Rotation (Degrees)
Pentasymmetron	5-fold	5.8	5.9
AAB-Heterotrimer	∥ Local 3-fold	1.1	1.3
	⊥ Local 3-fold	1.6	–
	AAB:AAB Interface	–	1.6, -2.8
	AAB:CCC Interface	–	-0.2
Trimer	3-fold	4.0	12.4

*The symbol ∥ indicates deviations parallel to the indicated symmetry axis, ⊥ indicates deviations perpendicular to the indicated axis.

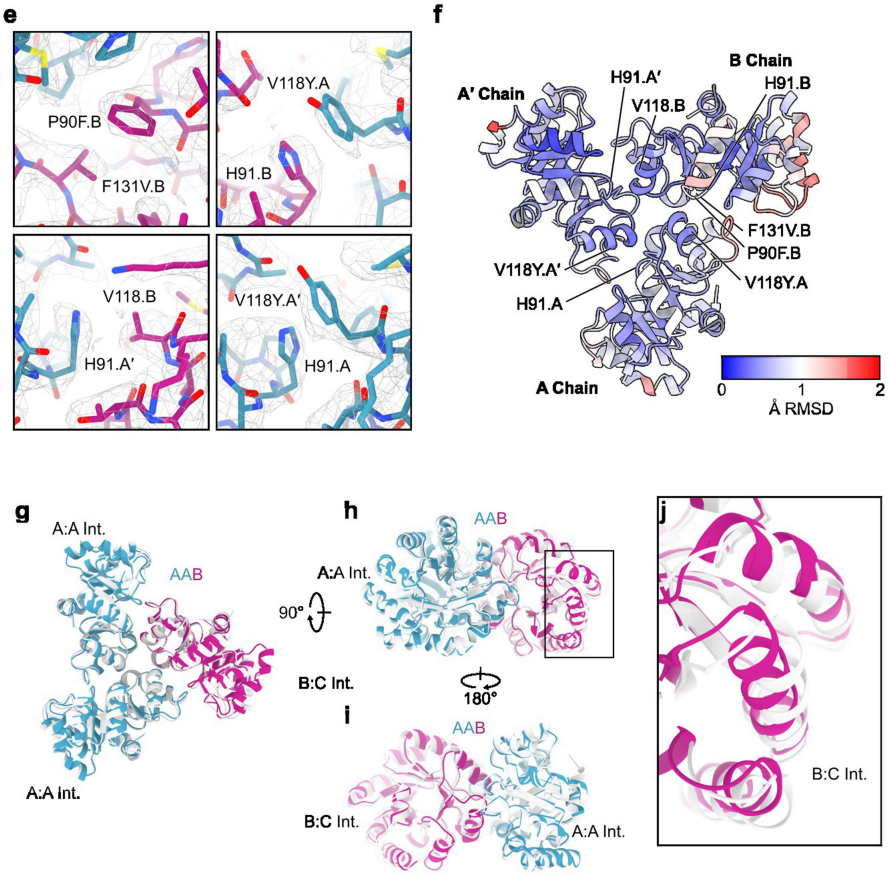

Extended Data Fig. 4 | See next page for caption.

Extended Data Fig. 4 | Structural details of GI_4-F7. a, Alignment of the complete cryoEM model to the design model. Major rigid-body DoF deviations are indicated with arrows. Two views of the asu are shown. Approximate locations of each inset (B, C, and D) are indicated. **b**, Comparison between the cryoEM model (left) and design model (right) of the newly designed nanocage (B-C) interface. *Top row*, M57 on the CCC-homotrimer changes rotamer to occupy a void in the interface in the design model. *Bottom row*, F57 on the B chain of the AAB heterotrimer packs against S187 of the CCC homotrimer in the cryoEM model, instead of A190 in the CCC homotrimer as in the design model. **c**, Comparison of the I3-01 (A-A) interface observed in the cryoEM model to a previously published structure (PDB ID 8ED3; ref. 78). *Top row*, slight rigid-body deviations from perfect two-fold symmetry in one copy of the A chain. *Bottom row*, very little deviation from perfect two-fold symmetry. **d**, Details of the density maps in the regions of the pseudosymmetry-generating mutations within the AAB heterotrimer interface. **e**, Pseudosymmetric heterotrimer colored by Cα-RMSD to the design model. The positions of the pseudosymmetry-generating mutations are indicated. **f**, Alignment of the AAB heterotrimer cryoEM model to the design model is viewed from the top, towards the center of the nanocage along the three-fold symmetry axis; **g**, from the side, tangential to the nanocage surface; and **h**, from the other side, tangential to the nanocage surface. The position of the A:A and newly designed B:C interfaces are indicated. **i**, Detail of the B side of the B:C interface, highlighting the most significant deviations from the design model. **j**, Deviations observed in the cryoEM reconstruction of GI_4-F7 compared to the design model.

a

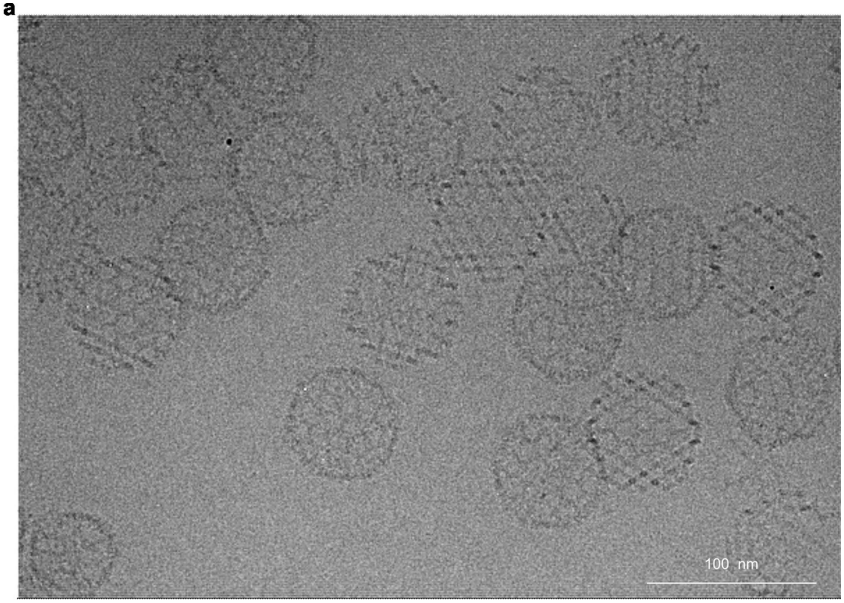

b

Component	Axis	Translation (Å)	Rotation (Degrees)
Pentasymmetron	Icosahedral 5-fold	7.7	7.2
AAB heterotrimer	∥ * Local 3-fold	1.3	1.8
	⊥ Local 3-fold	1.9	--
	AAB:AAB Interface	--	1.9, -3.6
	AAB:CCC Interface	--	0.3
Disymmetron	Icosahedral two-fold	10.0	8.2
ABB heterotrimer	∥ Local 3-fold	0.4	2.3
	⊥ Local 3-fold	1.3	--
	ABB:ABB Interface	--	-1.6
	ABB:CCC Interface	--	-0.8, 3.7
3× Trimer	Icosahedral 3-fold	6.5	5.4
CCC homotrimer	∥ Local 3-fold	0.0	-6.5
	⊥ Local 3-fold	1.23	--
	CCC:ABB Interface	--	0.3, -1.8
	CCC:AAB Interface	--	-0.6*

*The symbol ∥ indicates deviations parallel to the indicated symmetry axis, ⊥ indicates deviations perpendicular to the indicated axis.

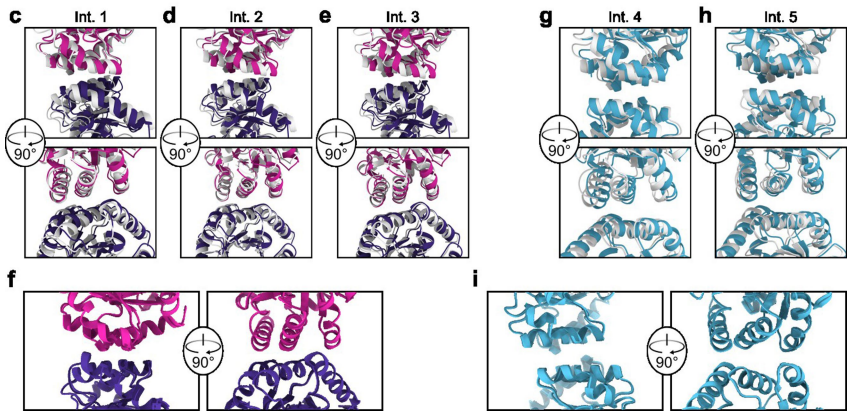

Extended Data Fig. 5 | See next page for caption.

Extended Data Fig. 5 | Discovery and structural details of GI_9-F7. a, CryoEM field view micrograph of samples enriched for GI_9-F7 by SEC purification. Both GI_9-F7 (large particles) and GI_4-F7 (e.g., bottom-left corner) are clearly visible. **b**, Table of deviations observed in the cryoEM reconstruction of GI_9-F7 compared to the design model. (**c-e**) Alignment of the GI_9-F7 design model chain B (magenta) and chain C (purple) protein-protein interface to the corresponding chains of the cryoEM model (gray). Each of the three interfaces between B and C chains in the asu are shown. **f**, The protein-protein interface between chain B and C from the cryoEM model of GI_4-F7 (light colors) aligned to the same interface from the cryoEM model of GI_9-F7 (dark colors). **g**, Alignment of design model to the cryoEM model for the I3-01 interface in the pentasymmetron and g, disymmetron. **h**, Alignment of the I3-01 interface from the cryoEM models of GI_4-F7 (light blue) and GI_9-F7 (dark blue).

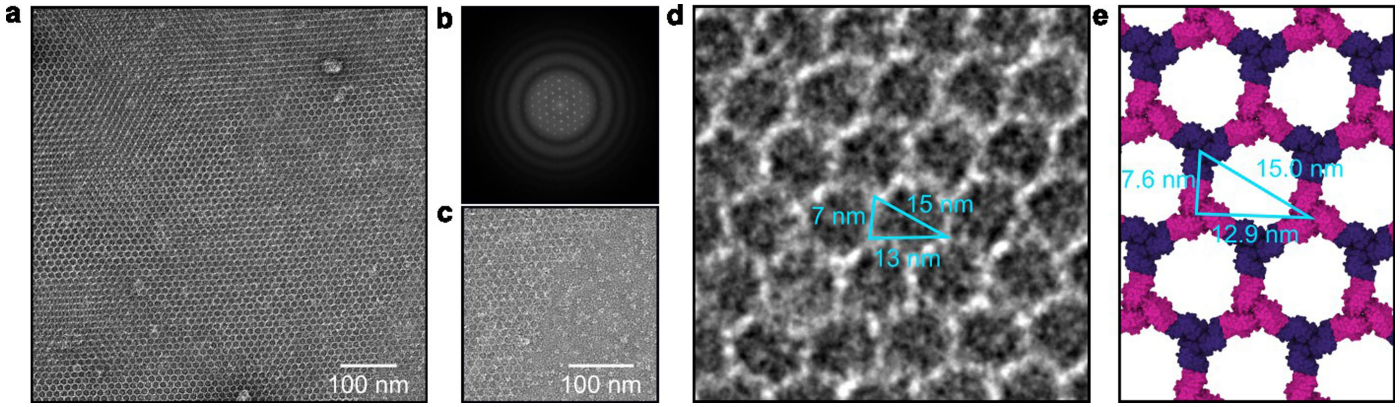

Extended Data Fig. 6 | Hexagonal 2D array characterization by negative stain EM. a, An example of the regular hexagonal array formed by mixing BBB and CCC homotrimers by negative stain EM. **b**, Power spectrum of the micrograph shown in panel A, confirming the periodic arrangement of the array. **c**, The edge of the array is jagged, with free trimeric components visible. **d**, Measurement of the array dimensions are consistent with **e**, the design model.

Extended Data Table 1 | Table of all single and double mutants and outcome

Single mutant	Assembles in lysate?
R17Y	Yes
T69E	Yes
T69G	Yes
T71A	Yes
T71D	Yes
T71E	Yes
T71K	Yes
T71L	Yes
T71N	Yes
T71Y	Yes
P90E	Yes
P90F	**No**
P90K	Yes
P90Q	Yes
P90R	Yes
H91C	Yes
H91D	Yes
H91F	Yes
H91G	Yes
H91I	Yes
H91S	Yes
D93R	Yes
M112P	**No**
M112Q	Yes
M112V	Yes
T113D	Yes
T113F	Yes
T113I	Yes
T113L	Yes
T113M	Yes
T113P	Yes
T113Q	Yes
T113V	Yes
P114Q	Yes
P114S	Yes
P114F	**No**
T115K	Yes
T116C	Yes
T116D	Yes
T116G	Yes
T116L	Yes
T116M	Yes
T116N	Yes
T116Q	Yes
T116S	Yes
T116T	Yes
T116W*	**No**
V118H	Yes
V118K	Yes
V118M	Yes
V118N	Yes
V118S	Yes
V118W	Yes
V118Y	**No**
K122D	Yes
K122E	Yes
F131E	Yes**
E134G	Yes
E134K	Yes
V135P	Yes
V136R	Yes
V136Y	Yes
V136W	Yes
Q139E	Yes
F140K	**No**
F140H	Yes
F140W	Yes
A143D	Yes
A143E	Yes
A143Y	Yes
P147A	Yes
P147D	Yes
P147H	Yes
P147M	Yes
P147R	Yes**
P147S	Yes
F148C	Yes
F148E	Yes
F148H	Yes
F148Q	Yes
F148Y	Yes

Double mutant	Assembles in lysate?
M112P/V136R	No
P90F/P147A	Yes
P114F/F131V	Yes
V118Y/H91I	Yes

* Mutant at three-fold position required screening in a tricistronic gene construct and was not pursued further.
** Did not assemble in one replicate or had a weak assembly band.

Extended Data Table 2 | CryoEM data collection and refinement statistics

	GI_4-F7 EMD 47034	GI_4-F7 (local refinement) PDB 9DND EMD 47036	GI_9-F7 EMD 47037	GI_9-F7 (local refinement) PDB 9DNE EMD 47038	GI_{16}-F7 EMD 47039
Data collection and processing					
Magnification	105,000	105,000	105,000	105,000	64,000
Voltage (kV)	300	300	300	300	300
Electron exposure (e^{-}/Å^2)	60	60	60	60	37
Defocus range (μm)	-0.5 – -2.5	-0.5 – -2.5	-0.5 – -2.5	-0.5 – -2.5	-0.5 – -3.5
Pixel size (Å)	0.843	0.843	0.843	0.843	1.42
Symmetry imposed	I	C1	I	C1	I
Initial particle images (no.)	154,574		18,611		1,226
Final particle images (no.)	120,979	984,020	1,956	795,360	1,083
Map resolution (Å)	4.4	3.1	6.7	4.0	14.9
FSC threshold	0.143	0.143	0.143	0.143	0.143
Refinement					
Map resolution (Å) FSC threshold		0.143		0.143	
Map sharpening *B* factor (Å^2)	-269	-143	-530	-138	
Model composition					
Non-hydrogen atoms		5,687		9,161	
Protein residues		813		1,827	
Ligands		0		0	
B factors (Å^2)					
Protein		15.53		73.75	
Ligand		N/A		N/A	
Validation					
MolProbity score		1.9		1.06	
Clashscore		5.86		0.71	
Poor rotamers (%)		2.94		0.13	
Ramachandran plot					
Favored (%)		96.52		98.95	
Allowed (%)		3.11		0.5	
Disallowed (%)		0.37		0.55	

Extended Data Table 3 | DLS results obtained from assembly reactions corresponding to T numbers 4 to 100

T	Mean Z-Ave. dia. (nm)	StdDev Z-Ave. dia. (nm)	PDI
4	47.5	0.4	0.048
9	69.9	0.5	0.154
16	95	1	0.121
25	113.2	0.5	0.127
36	129	2	0.134
49	148	2	0.136
64	162	1	0.136
81	174	1	0.126
100	189	1	0.133

nature portfolio

Corresponding author(s): Neil King

Last updated by author(s): Quinton Dowling

Reporting Summary

Nature Portfolio wishes to improve the reproducibility of the work that we publish. This form provides structure for consistency and transparency in reporting. For further information on Nature Portfolio policies, see our Editorial Policies and the Editorial Policy Checklist.

Statistics

For all statistical analyses, confirm that the following items are present in the figure legend, table legend, main text, or Methods section.

n/a	Confirmed	
☐	☒	The exact sample size (*n*) for each experimental group/condition, given as a discrete number and unit of measurement
☐	☒	A statement on whether measurements were taken from distinct samples or whether the same sample was measured repeatedly
☒	☐	The statistical test(s) used AND whether they are one- or two-sided *Only common tests should be described solely by name; describe more complex techniques in the Methods section.*
☒	☐	A description of all covariates tested
☒	☐	A description of any assumptions or corrections, such as tests of normality and adjustment for multiple comparisons
☐	☒	A full description of the statistical parameters including central tendency (e.g. means) or other basic estimates (e.g. regression coefficient) AND variation (e.g. standard deviation) or associated estimates of uncertainty (e.g. confidence intervals)
☒	☐	For null hypothesis testing, the test statistic (e.g. *F*, *t*, *r*) with confidence intervals, effect sizes, degrees of freedom and *P* value noted *Give P values as exact values whenever suitable.*
☒	☐	For Bayesian analysis, information on the choice of priors and Markov chain Monte Carlo settings
☒	☐	For hierarchical and complex designs, identification of the appropriate level for tests and full reporting of outcomes
☒	☐	Estimates of effect sizes (e.g. Cohen's *d*, Pearson's *r*), indicating how they were calculated

Our web collection on statistics for biologists contains articles on many of the points above.

Software and code

Policy information about availability of computer code

Data collection	Computational design was performed with the Rosetta 3.1 software suite. Custom XML and Bash scripts used to execute design in Rosetta are available on GitHub (https://github.com/quecloud/Hierarchical-pseudosymmetric-nanocage-design) and Zenodo DOI: 10.5281/zenodo.13958626. Cryo EM data were collected with Leginon v3.5. Negative stain data were collected with EPU v2.12.1.2782REL
Data analysis	Data were analyzed with Matplotlib (v3.3.3). Coevolution analysis was performed via the GREMLIN web portal (https://gremlin.bakerlab.org/). Cryo EM data were processed with CryoSPARC v4.4.0, Relion v3.0, Coot v1.0.1, and Chimera v1.7.1. Flow cytometry data were analyzed using FlowJo v10 (BD Biosciences). All data were processed and plotted using Python 3.8.8, Matplotlib 3.3.4, and Seaborn 0.11.1.

For manuscripts utilizing custom algorithms or software that are central to the research but not yet described in published literature, software must be made available to editors and reviewers. We strongly encourage code deposition in a community repository (e.g. GitHub). See the Nature Portfolio guidelines for submitting code & software for further information.

Data

Policy information about availability of data

All manuscripts must include a data availability statement. This statement should provide the following information, where applicable:

- Accession codes, unique identifiers, or web links for publicly available datasets
- A description of any restrictions on data availability
- For clinical datasets or third party data, please ensure that the statement adheres to our policy

Further information and requests for resources and reagents should be directed to and will be fulfilled by the corresponding author (neilking@uw.edu). EM maps and models for GI4-F7 are available from the Electron Microscopy Data Bank (EMD) under the accession number EMD-47034, local refinements for GI4-F7 under the accession number EMD-47036 and also available in the Protein Data Bank (PDB) under the accession number 9DND, EM maps and models for GI9-F7 under the accession number EMD-47037, local refinements for GI9-F7 under PDB ID 9DNE and EMD-47038, and EM maps and models for GI16-F7 under the accession number EMD-47039. Structural data for the KDPG from T. maritima, the lumazine synthase from M. loti, and I3-01 are available in the Protein Data Bank (PDB IDs 1WA3, 2OBX, and 8ED3, respectively). All other data are available in the manuscript or the supplementary materials.

Research involving human participants, their data, or biological material

Policy information about studies with human participants or human data. See also policy information about sex, gender (identity/presentation), and sexual orientation and race, ethnicity and racism.

Reporting on sex and gender	NA
Reporting on race, ethnicity, or other socially relevant groupings	NA
Population characteristics	NA
Recruitment	NA
Ethics oversight	NA

Note that full information on the approval of the study protocol must also be provided in the manuscript.

Field-specific reporting

Please select the one below that is the best fit for your research. If you are not sure, read the appropriate sections before making your selection.

☒ Life sciences ☐ Behavioural & social sciences ☐ Ecological, evolutionary & environmental sciences

For a reference copy of the document with all sections, see nature.com/documents/nr-reporting-summary-flat.pdf

Life sciences study design

All studies must disclose on these points even when the disclosure is negative.

Sample size	In vitro DLS measurements were collected in triplicate on a single particle assembly to provide an estimate of the measurement standard deviation. This is sufficient because no statistical comparison is made between the measurements, rather the data demonstrate the effect of increasing size with changing assembly stoichiomentry.
Data exclusions	No data were excluded
Replication	All in vitro experiments were replicated at least once
Randomization	Randomization was not necessary for these experiments. The analytical methods used herein are not susceptible to bias from lack of randomization.
Blinding	No blinding was necessary. The analytical methods used herein are not susceptible to bias from lack of blinding when no data are excluded from the analysis.

Behavioural & social sciences study design

All studies must disclose on these points even when the disclosure is negative.

Study description	*Briefly describe the study type including whether data are quantitative, qualitative, or mixed-methods (e.g. qualitative cross-sectional,*

Study description	*quantitative experimental, mixed-methods case study).*
Research sample	*State the research sample (e.g. Harvard university undergraduates, villagers in rural India) and provide relevant demographic information (e.g. age, sex) and indicate whether the sample is representative. Provide a rationale for the study sample chosen. For studies involving existing datasets, please describe the dataset and source.*
Sampling strategy	*Describe the sampling procedure (e.g. random, snowball, stratified, convenience). Describe the statistical methods that were used to predetermine sample size OR if no sample-size calculation was performed, describe how sample sizes were chosen and provide a rationale for why these sample sizes are sufficient. For qualitative data, please indicate whether data saturation was considered, and what criteria were used to decide that no further sampling was needed.*
Data collection	*Provide details about the data collection procedure, including the instruments or devices used to record the data (e.g. pen and paper, computer, eye tracker, video or audio equipment) whether anyone was present besides the participant(s) and the researcher, and whether the researcher was blind to experimental condition and/or the study hypothesis during data collection.*
Timing	*Indicate the start and stop dates of data collection. If there is a gap between collection periods, state the dates for each sample cohort.*
Data exclusions	*If no data were excluded from the analyses, state so OR if data were excluded, provide the exact number of exclusions and the rationale behind them, indicating whether exclusion criteria were pre-established.*
Non-participation	*State how many participants dropped out/declined participation and the reason(s) given OR provide response rate OR state that no participants dropped out/declined participation.*
Randomization	*If participants were not allocated into experimental groups, state so OR describe how participants were allocated to groups, and if allocation was not random, describe how covariates were controlled.*

Ecological, evolutionary & environmental sciences study design

All studies must disclose on these points even when the disclosure is negative.

Study description	*Briefly describe the study. For quantitative data include treatment factors and interactions, design structure (e.g. factorial, nested, hierarchical), nature and number of experimental units and replicates.*
Research sample	*Describe the research sample (e.g. a group of tagged Passer domesticus, all Stenocereus thurberi within Organ Pipe Cactus National Monument), and provide a rationale for the sample choice. When relevant, describe the organism taxa, source, sex, age range and any manipulations. State what population the sample is meant to represent when applicable. For studies involving existing datasets, describe the data and its source.*
Sampling strategy	*Note the sampling procedure. Describe the statistical methods that were used to predetermine sample size OR if no sample-size calculation was performed, describe how sample sizes were chosen and provide a rationale for why these sample sizes are sufficient.*
Data collection	*Describe the data collection procedure, including who recorded the data and how.*
Timing and spatial scale	*Indicate the start and stop dates of data collection, noting the frequency and periodicity of sampling and providing a rationale for these choices. If there is a gap between collection periods, state the dates for each sample cohort. Specify the spatial scale from which the data are taken*
Data exclusions	*If no data were excluded from the analyses, state so OR if data were excluded, describe the exclusions and the rationale behind them, indicating whether exclusion criteria were pre-established.*
Reproducibility	*Describe the measures taken to verify the reproducibility of experimental findings. For each experiment, note whether any attempts to repeat the experiment failed OR state that all attempts to repeat the experiment were successful.*
Randomization	*Describe how samples/organisms/participants were allocated into groups. If allocation was not random, describe how covariates were controlled. If this is not relevant to your study, explain why.*
Blinding	*Describe the extent of blinding used during data acquisition and analysis. If blinding was not possible, describe why OR explain why blinding was not relevant to your study.*

Did the study involve field work? ☐ Yes ☐ No

Field work, collection and transport

Field conditions	*Describe the study conditions for field work, providing relevant parameters (e.g. temperature, rainfall).*
Location	*State the location of the sampling or experiment, providing relevant parameters (e.g. latitude and longitude, elevation, water depth).*
Access & import/export	*Describe the efforts you have made to access habitats and to collect and import/export your samples in a responsible manner and in*

Access & import/export	*compliance with local, national and international laws, noting any permits that were obtained (give the name of the issuing authority, the date of issue, and any identifying information).*
Disturbance	*Describe any disturbance caused by the study and how it was minimized.*

Reporting for specific materials, systems and methods

We require information from authors about some types of materials, experimental systems and methods used in many studies. Here, indicate whether each material, system or method listed is relevant to your study. If you are not sure if a list item applies to your research, read the appropriate section before selecting a response.

Materials & experimental systems

n/a	Involved in the study
☐	☒ Antibodies
☐	☒ Eukaryotic cell lines
☒	☐ Palaeontology and archaeology
☒	☐ Animals and other organisms
☒	☐ Clinical data
☒	☐ Dual use research of concern
☒	☐ Plants

Methods

n/a	Involved in the study
☒	☐ ChIP-seq
☐	☒ Flow cytometry
☒	☐ MRI-based neuroimaging

Antibodies

Antibodies used	Polyclonal goat anti-human IgG F(ab')2 (Southern Biotech; Cat # 2042-01; Lot # F2323-MH74)
Validation	Antibody has been validated by the manufacturer and was additionally titrated for use in the activation assay.

Eukaryotic cell lines

Policy information about cell lines and Sex and Gender in Research

Cell line source(s)	COVA2-15 IgG RAMOS cell line was provided by the Marit van Gils lab, Amsterdam University Medical Center. Ramos (RA 1) is a B lymphocyte cell line that was derived from a 3-year-old, White, male patient with Burkitt's Lymphoma (American). The cell line was modified through lentiviral transduction to express the SARS-CoV-2 specific IgG antibody COVA2-15 as a membrane-bound B cell receptor.
Authentication	Cell line was not authenticated.
Mycoplasma contamination	Cell line was not tested for mycoplasma contamination.
Commonly misidentified lines (See ICLAC register)	The COVA2-15 IgG RAMOS cell line is not a commonly misidentified cell line.

Palaeontology and Archaeology

Specimen provenance	*Provide provenance information for specimens and describe permits that were obtained for the work (including the name of the issuing authority, the date of issue, and any identifying information). Permits should encompass collection and, where applicable, export.*
Specimen deposition	*Indicate where the specimens have been deposited to permit free access by other researchers.*
Dating methods	*If new dates are provided, describe how they were obtained (e.g. collection, storage, sample pretreatment and measurement), where they were obtained (i.e. lab name), the calibration program and the protocol for quality assurance OR state that no new dates are provided.*

☐ Tick this box to confirm that the raw and calibrated dates are available in the paper or in Supplementary Information.

Ethics oversight	*Identify the organization(s) that approved or provided guidance on the study protocol, OR state that no ethical approval or guidance was required and explain why not.*

Note that full information on the approval of the study protocol must also be provided in the manuscript.

Animals and other research organisms

Policy information about studies involving animals; ARRIVE guidelines recommended for reporting animal research, and Sex and Gender in Research

Laboratory animals	*For laboratory animals, report species, strain and age OR state that the study did not involve laboratory animals.*
Wild animals	*Provide details on animals observed in or captured in the field; report species and age where possible. Describe how animals were caught and transported and what happened to captive animals after the study (if killed, explain why and describe method; if released, say where and when) OR state that the study did not involve wild animals.*
Reporting on sex	*Indicate if findings apply to only one sex; describe whether sex was considered in study design, methods used for assigning sex. Provide data disaggregated for sex where this information has been collected in the source data as appropriate; provide overall numbers in this Reporting Summary. Please state if this information has not been collected. Report sex-based analyses where performed, justify reasons for lack of sex-based analysis.*
Field-collected samples	*For laboratory work with field-collected samples, describe all relevant parameters such as housing, maintenance, temperature, photoperiod and end-of-experiment protocol OR state that the study did not involve samples collected from the field.*
Ethics oversight	*Identify the organization(s) that approved or provided guidance on the study protocol, OR state that no ethical approval or guidance was required and explain why not.*

Note that full information on the approval of the study protocol must also be provided in the manuscript.

Clinical data

Policy information about clinical studies

All manuscripts should comply with the ICMJE guidelines for publication of clinical research and a completed CONSORT checklist must be included with all submissions.

Clinical trial registration	*Provide the trial registration number from ClinicalTrials.gov or an equivalent agency.*
Study protocol	*Note where the full trial protocol can be accessed OR if not available, explain why.*
Data collection	*Describe the settings and locales of data collection, noting the time periods of recruitment and data collection.*
Outcomes	*Describe how you pre-defined primary and secondary outcome measures and how you assessed these measures.*

Dual use research of concern

Policy information about dual use research of concern

Hazards

Could the accidental, deliberate or reckless misuse of agents or technologies generated in the work, or the application of information presented in the manuscript, pose a threat to:

No	Yes	
☒	☐	Public health
☒	☐	National security
☒	☐	Crops and/or livestock
☒	☐	Ecosystems
☒	☐	Any other significant area

Experiments of concern

Does the work involve any of these experiments of concern:

No	Yes	
☒	☐	Demonstrate how to render a vaccine ineffective
☒	☐	Confer resistance to therapeutically useful antibiotics or antiviral agents
☒	☐	Enhance the virulence of a pathogen or render a nonpathogen virulent
☒	☐	Increase transmissibility of a pathogen
☒	☐	Alter the host range of a pathogen
☒	☐	Enable evasion of diagnostic/detection modalities
☒	☐	Enable the weaponization of a biological agent or toxin
☒	☐	Any other potentially harmful combination of experiments and agents

Plants

Seed stocks

Report on the source of all seed stocks or other plant material used. If applicable, state the seed stock centre and catalogue number. If plant specimens were collected from the field, describe the collection location, date and sampling procedures.

Novel plant genotypes

Describe the methods by which all novel plant genotypes were produced. This includes those generated by transgenic approaches, gene editing, chemical/radiation-based mutagenesis and hybridization. For transgenic lines, describe the transformation method, the number of independent lines analyzed and the generation upon which experiments were performed. For gene-edited lines, describe the editor used, the endogenous sequence targeted for editing, the targeting guide RNA sequence (if applicable) and how the editor was applied.

Authentication

Describe any authentication procedures for each seed stock used or novel genotype generated. Describe any experiments used to assess the effect of a mutation and, where applicable, how potential secondary effects (e.g. second site T-DNA insertions, mosiacism, off-target gene editing) were examined.

ChIP-seq

Data deposition

☐ Confirm that both raw and final processed data have been deposited in a public database such as GEO.

☐ Confirm that you have deposited or provided access to graph files (e.g. BED files) for the called peaks.

Data access links
May remain private before publication.

For "Initial submission" or "Revised version" documents, provide reviewer access links. For your "Final submission" document, provide a link to the deposited data.

Files in database submission

Provide a list of all files available in the database submission.

Genome browser session
(e.g. UCSC)

Provide a link to an anonymized genome browser session for "Initial submission" and "Revised version" documents only, to enable peer review. Write "no longer applicable" for "Final submission" documents.

Methodology

Replicates

Describe the experimental replicates, specifying number, type and replicate agreement.

Sequencing depth

Describe the sequencing depth for each experiment, providing the total number of reads, uniquely mapped reads, length of reads and whether they were paired- or single-end.

Antibodies

Describe the antibodies used for the ChIP-seq experiments; as applicable, provide supplier name, catalog number, clone name, and lot number.

Peak calling parameters

Specify the command line program and parameters used for read mapping and peak calling, including the ChIP, control and index files used.

Data quality

Describe the methods used to ensure data quality in full detail, including how many peaks are at FDR 5% and above 5-fold enrichment.

Software

Describe the software used to collect and analyze the ChIP-seq data. For custom code that has been deposited into a community repository, provide accession details.

Flow Cytometry

Plots

Confirm that:

☒ The axis labels state the marker and fluorochrome used (e.g. CD4-FITC).

☒ The axis scales are clearly visible. Include numbers along axes only for bottom left plot of group (a 'group' is an analysis of identical markers).

☒ All plots are contour plots with outliers or pseudocolor plots.

☒ A numerical value for number of cells or percentage (with statistics) is provided.

Methodology

Sample preparation	For Ca2+ flux experiments, cells were loaded with FuraRed cell-permeable dye (ThermoFisher) for 30 minutes in RPMI1640 supplemented with 10% fetal clone II, 1% L-glutamax, and 1% penicillin-streptomycin (complete media) at a cell concentration of 1×107 per mL. Cells were then washed with 10× volume complete media, resuspended at 2×106 cells per mL in complete media, and aliquoted at 0.25 mL into individual FACS tubes. Samples were kept at room temperature and then warmed in a 37 °C bath for 3 minutes immediately before use
Instrument	Attune CytPix flow cytometer (ThermoFisher), Model 0A48663, Lasers:BRVY
Software	Attune Cytometric Software v6.2.0 was used for acquisition. FlowJo v10 (BD Biosciences) was used for analysis.
Cell population abundance	~97% of cells expressed the GFP reporter indicating transduction with the COVA2-15 IgG B cell receptor.
Gating strategy	Cells were gated by size (SSC-A vs FSC-A), singlets (FSC-H vs FSC-A), and for GFP expression for analysis. The FuraRed ratio of bound (fluorescence in VL3) and unbound (fluorescence in BL1) Ca2+ was used for analysis using FlowJo v10 (BD Biosciences).

☒ Tick this box to confirm that a figure exemplifying the gating strategy is provided in the Supplementary Information.

Magnetic resonance imaging

Experimental design

Design type	*Indicate task or resting state; event-related or block design.*
Design specifications	*Specify the number of blocks, trials or experimental units per session and/or subject, and specify the length of each trial or block (if trials are blocked) and interval between trials.*
Behavioral performance measures	*State number and/or type of variables recorded (e.g. correct button press, response time) and what statistics were used to establish that the subjects were performing the task as expected (e.g. mean, range, and/or standard deviation across subjects).*

Acquisition

Imaging type(s)	*Specify: functional, structural, diffusion, perfusion.*
Field strength	*Specify in Tesla*
Sequence & imaging parameters	*Specify the pulse sequence type (gradient echo, spin echo, etc.), imaging type (EPI, spiral, etc.), field of view, matrix size, slice thickness, orientation and TE/TR/flip angle.*
Area of acquisition	*State whether a whole brain scan was used OR define the area of acquisition, describing how the region was determined.*

Diffusion MRI ☐ Used ☐ Not used

Preprocessing

Preprocessing software	*Provide detail on software version and revision number and on specific parameters (model/functions, brain extraction, segmentation, smoothing kernel size, etc.).*
Normalization	*If data were normalized/standardized, describe the approach(es): specify linear or non-linear and define image types used for transformation OR indicate that data were not normalized and explain rationale for lack of normalization.*
Normalization template	*Describe the template used for normalization/transformation, specifying subject space or group standardized space (e.g. original Talairach, MNI305, ICBM152) OR indicate that the data were not normalized.*

Noise and artifact removal

Describe your procedure(s) for artifact and structured noise removal, specifying motion parameters, tissue signals and physiological signals (heart rate, respiration).

Volume censoring

Define your software and/or method and criteria for volume censoring, and state the extent of such censoring.

Statistical modeling & inference

Model type and settings

Specify type (mass univariate, multivariate, RSA, predictive, etc.) and describe essential details of the model at the first and second levels (e.g. fixed, random or mixed effects; drift or auto-correlation).

Effect(s) tested

Define precise effect in terms of the task or stimulus conditions instead of psychological concepts and indicate whether ANOVA or factorial designs were used.

Specify type of analysis: ☐ Whole brain ☐ ROI-based ☐ Both

Statistic type for inference

Specify voxel-wise or cluster-wise and report all relevant parameters for cluster-wise methods.

(See Eklund et al. 2016)

Correction

Describe the type of correction and how it is obtained for multiple comparisons (e.g. FWE, FDR, permutation or Monte Carlo).

Models & analysis

n/a	Involved in the study
☐	☐ Functional and/or effective connectivity
☐	☐ Graph analysis
☐	☐ Multivariate modeling or predictive analysis

Functional and/or effective connectivity

Report the measures of dependence used and the model details (e.g. Pearson correlation, partial correlation, mutual information).

Graph analysis

Report the dependent variable and connectivity measure, specifying weighted graph or binarized graph, subject- or group-level, and the global and/or node summaries used (e.g. clustering coefficient, efficiency, etc.).

Multivariate modeling and predictive analysis

Specify independent variables, features extraction and dimension reduction, model, training and evaluation metrics.